Multifractal subgrid-scale modeling for large-eddy simulation. II. Backscatter limiting and *a posteriori* evaluation

Gregory C. Burton[a)]
Laboratory for Turbulence and Combustion and W. M. Keck Laboratory for Computational Fluid Dynamics, Department of Aerospace Engineering, The University of Michigan, Ann Arbor, Michigan 48109-2140

Werner J. A. Dahm
Laboratory for Turbulence and Combustion (LTC), Department of Aerospace Engineering, The University of Michigan, Ann Arbor, Michigan 48109-2140

(Received 27 April 2005; accepted 13 May 2005; published online 13 July 2005)

Results are presented from *a posteriori* evaluations of momentum and energy transfer between the resolved and subgrid scales when the multifractal subgrid-scale model from Part I is implemented in a flow solver for large-eddy simulations of turbulent flows. The multifractal subgrid-stress model is used to evaluate the subgrid part τ_{ij}^* of the stress tensor, with the resolved part $\overline{\bar{u}_i\bar{u}_j}$ evaluated by an explicit filter. It is shown that the corresponding subgrid and resolved contributions $\mathcal{P}^*$ and $\mathcal{P}^R$ to the resolved-scale energetics produce extremely accurate results for the combined subgrid energy production field $\mathcal{P}(\mathbf{x},t)$. A separate backscatter limiter is developed here that removes spurious energy introduced in the resolved scales by including physical backscatter, without sacrificing the high fidelity in the stress and energy production fields produced by the multifractal subgrid-scale model. This limiter makes small reductions only to those components of the stress that contribute to backscatter, and principally in locations where the gradients are large and thus the energy introduced by numerical errors is also largest. Control of the energy introduced by numerical error is thus accomplished in a manner that leaves the modeling of the subgrid-scale turbulence largely unchanged. The multifractal subgrid-scale model and the backscatter limiter are then implemented in a flow solver and shown to provide stable and accurate results in *a posteriori* tests based on large-eddy simulations of forced homogeneous isotropic turbulence at cell Reynolds numbers ranging from $160 \leqslant Re_\Delta \leqslant 10^6$, as well as in simulations of decaying turbulence where the model and the limiter must adjust to the changing subgrid conditions. © *2005 American Institute of Physics*. [DOI: 10.1063/1.1965094]

I. INTRODUCTION

A companion paper,[1] herein referred to as Part I, presented a new approach to modeling the subgrid stresses for large-eddy simulation (LES) of turbulent flows, based on the multifractal structure of the subgrid enstrophy field at inertial-range scales. That work outlined a method for modeling the subgrid vorticity field $\boldsymbol{\omega}^{sgs}(\mathbf{x},t)$ with a multifractal representation, and from this derived expressions for the subgrid velocity components $u_i^{sgs}(\mathbf{x},t)$ and the associated subgrid stress component fields $\tau_{ij}^*(\mathbf{x},t)$. Part I also presented results from *a priori* tests in which the multifractal subgrid-scale model was compared against direct numerical simulation (DNS) data for homogeneous isotropic turbulence. Those results showed that the model recovered the filtered subgrid velocity fields $\overline{u_i^{sgs}}$, the subgrid stresses τ_{ij}^*, and the subgrid energy production field $\mathcal{P}^*$ with significantly higher fidelity than is typically reported for models based on traditional eddy-viscosity or mixed scale-similarity approaches.

However, when any subgrid-stress model is implemented in an LES flow solver, then the results will reflect not only the fidelity of the subgrid-stress model, but also the effects of purely numerical errors introduced by the flow solver itself. These numerical errors include discretization and truncation errors introduced by discrete representations in the solver, aliasing errors introduced by nonlinear terms due to the finite resolution of the computations, and filtering and commutation errors introduced by implicit or explicit filters used in the solver. The aliasing errors, which arise from the inherent under-resolution in LES, inject spurious energy into the resolved scales of the flow and thereby act to destabilize the simulation. This spurious energy transfer is in addition to the natural energy exchange between the resolved and subgrid scales from physical interactions between the stress and strain-rate fields in the turbulent flow. Thus even with an "ideal" subgrid-scale turbulence model, namely one that in the absence of numerical errors always produces the exact subgrid-stress field $\tau_{ij}(\mathbf{x},t)$ when provided with exact resolved velocity field data, the flow solver must also include a means to remove the additional energy to remain stable and obtain physically realistic results.

Against this background, subgrid-scale models have often been treated as much as a means of stabilizing computations by removing the additional energy as they are a means

[a)]Present address: Center for Turbulence Research, Stanford University, Stanford, CA 94305-3035.

to model the physical interactions that give rise to the actual energy transfer between the resolved and subgrid scales in turbulent flows. Indeed the distinction between these two roles of a subgrid-scale model is often not articulated. Thus subgrid models have sometimes been deemed successful if they produce the correct overall level of energy in the resolved scales, even if they fail to provide high fidelity in the detailed spatial and temporal transport of momentum and energy within the flow.

In this paper, it is shown that the spurious energy introduced in the resolved scales by errors inherent in the numerics of a flow solver may be removed in a manner that does not significantly sacrifice the fidelity of the detailed spatial and temporal transport of momentum and energy in the $\tau_{ij}^*(\mathbf{x},t)$ and $\mathcal{P}^*(\mathbf{x},t)$ fields produced by the multifractal subgrid-scale model from Part I. By a relatively small reduction to only those stress components that contribute to backscatter of energy from the subgrid scales to the resolved scales—i.e., by limiting backscatter, principally in regions where the errors are largest—the control of spurious energy is accomplished in a manner that leaves the modeling of the subgrid-scale turbulence largely unchanged. This effectively separates the role of the subgrid model from the additional burden of controlling the numerical error. The multifractal model and backscatter limiter are then implemented in a flow solver and shown to provide stable and accurate results in large-eddy simulations on a 32^3 grid of forced homogeneous isotropic turbulence at cell Reynolds numbers ranging from $Re_\Delta \approx 160$, for which filtered DNS data are available for comparison, to the highest values tested, approaching $Re_\Delta \approx 10^6$. The multifractal subgrid-scale model and the backscatter limiter are furthermore shown to provide stable and accurate results in LES of decaying homogeneous isotropic turbulence, where both the model and the limiter must adjust to the changing subgrid conditions.

II. MOMENTUM AND ENERGY TRANSPORT IN LES

A. Traditional form of the momentum equation

The most commonly used form of the momentum equation for large-eddy simulations of incompressible flows is

$$\frac{\partial \bar{u}_i}{\partial t} + \frac{\partial}{\partial x_j}\bar{u}_i\bar{u}_j - \nu\frac{\partial^2 \bar{u}_i}{\partial x_j\,\partial x_j} + \frac{1}{\rho}\frac{\partial \bar{p}}{\partial x_i} = -\frac{\partial}{\partial x_j}\tau_{ij}, \tag{1}$$

where the subgrid stress is given by $\tau_{ij} \equiv \overline{u_i u_j} - \bar{u}_i\bar{u}_j$. Since the $\overline{u_i u_j}$ term is typically not available to the flow solver, large-eddy simulations based on this form of the momentum equation generally model both terms of τ_{ij} as a single entity, often with an eddy-viscosity model or some other representation. Irrespective of the subgrid model used for τ_{ij}, the kinetic energy $\mathcal{E}(\mathbf{x},t) \equiv \frac{1}{2}\bar{u}_i\bar{u}_i$ of the resolved field then follows as

$$\frac{\partial \mathcal{E}}{\partial t} + \bar{u}_j\frac{\partial \mathcal{E}}{\partial x_j} = \frac{\partial}{\partial x_j}[\mathcal{Q}_j] - \mathcal{D} - \mathcal{P}. \tag{2}$$

Note that the flux vector $\mathcal{Q}_j$, given by

$$\mathcal{Q}_j(\mathbf{x},t) \equiv -\left[\bar{u}_i\tau_{ij} + \bar{u}_j\frac{\bar{p}}{\rho} - \nu\frac{\partial \mathcal{E}}{\partial x_j}\right], \tag{3}$$

appears in (2) in divergence form and thus does not contribute to energy transfer between the resolved and subgrid scales. The viscous dissipation of resolved kinetic energy, given by

$$\mathcal{D}(\mathbf{x},t) \equiv \nu\frac{\partial \bar{u}_i}{\partial x_j}\frac{\partial \bar{u}_i}{\partial x_j}, \tag{4}$$

scales in (2) relative to the inertial transport of $\mathcal{E}$ with the cell Reynolds number as Re_Δ^{-1}, and thus is a negligible contributor to the energy balance at large Re_Δ. The remaining term

$$\mathcal{P}(\mathbf{x},t) \equiv -\tau_{ij}\bar{S}_{ij} \tag{5}$$

is often called the "subgrid energy production," where $\bar{S}_{ij}$ is the resolved strain-rate tensor defined as

$$\bar{S}_{ij} \equiv \frac{1}{2}\left(\frac{\partial \bar{u}_i}{\partial x_j} + \frac{\partial \bar{u}_j}{\partial x_i}\right). \tag{6}$$

$\mathcal{P}(\mathbf{x},t)$ gives the inertial transfer of kinetic energy between the resolved and subgrid fields due to vortex line stretching in one field by the strain rate field imposed from the other.

B. Present form of the momentum equation

While (1) is the more widely used form of the momentum equation, an alternative is to equivalently express this as

$$\frac{\partial \bar{u}_i}{\partial t} + \frac{\partial}{\partial x_j}\overline{\bar{u}_i\bar{u}_j} + \frac{1}{\rho}\frac{\partial \bar{p}}{\partial x_i} - \nu\frac{\partial^2 \bar{u}_i}{\partial x_j\,\partial x_j} = -\frac{\partial}{\partial x_j}\tau_{ij}^*, \tag{7}$$

where the long overbar represents an explicit filter on the product $\bar{u}_i\bar{u}_j$ of the resolved velocity components. The corresponding subgrid stress τ_{ij}^* in (7) is then given in terms of the resolved and subgrid velocity fields by

$$\tau_{ij}^* \equiv \overline{\bar{u}_i u_j^{sgs}} + \overline{u_i^{sgs}\bar{u}_j} + \overline{u_i^{sgs}u_j^{sgs}}. \tag{8}$$

In principle, τ_{ij}^* could also be modeled as a single entity by an eddy-viscosity model or some other representation. However, unlike τ_{ij} in Sec. II A, τ_{ij}^* in (8) involves only terms which depend directly on the subgrid velocity field. A further alternative is thus to develop a subgrid model that can explicitly evaluate the contributions of the subgrid velocity fields u_i^{sgs} to each of the three terms in (8). Such a model for the subgrid velocities was developed in Part I from a multifractal cascade representation for the subgrid vorticity field.

The kinetic energy $\mathcal{E}(\mathbf{x},t)$ in the resolved field then follows from (7) as

$$\frac{\partial \mathcal{E}}{\partial t} + \bar{u}_j\frac{\partial \mathcal{E}}{\partial x_j} = \frac{\partial}{\partial x_j}[\mathcal{R}_j] - \mathcal{D} - \mathcal{P}, \tag{9}$$

where the corresponding flux vector $\mathcal{R}_j$ is now given by

$$\mathcal{R}_j(\mathbf{x},t) \equiv -\left[\bar{u}_i(\overline{\bar{u}_i\bar{u}_j} + \tau_{ij}^*) - \bar{u}_j\mathcal{E} + \bar{u}_j\frac{\bar{p}}{\rho} - \nu\frac{\partial \mathcal{E}}{\partial x_j}\right]. \tag{10}$$

The viscous dissipation $\mathcal{D}$ of resolved kinetic energy in (9) is still given by (4), and thus remains negligible at large Re_Δ.

However, now the subgrid energy production $\mathcal{P}$ is

$$\mathcal{P}(\mathbf{x},t) \equiv -(\overline{\bar{u}_i\bar{u}_j} + \tau_{ij}^*)\bar{S}_{ij}, \tag{11}$$

which can be separated into subgrid and resolved parts as $\mathcal{P} \equiv \mathcal{P}^* + \mathcal{P}^R$, with

$$\mathcal{P}^*(\mathbf{x},t) \equiv -\tau_{ij}^*\bar{S}_{ij} \tag{12}$$

giving the contribution to subgrid energy production due to the subgrid stress τ_{ij}^* in (8), and

$$\mathcal{P}^R(\mathbf{x},t) \equiv -\overline{\bar{u}_i\bar{u}_j}\bar{S}_{ij} \tag{13}$$

giving the contribution to subgrid energy production by the resolved stress $\overline{\bar{u}_i\bar{u}_j}$. The contribution $\mathcal{P}^R$ to the total energy transfer, termed "false" dissipation by Lund,[2] in fact gives the energy exchange due to interaction between the filtered components of the resolved velocity field and the resolved strain-rate field, as discussed by Leonard.[3]

The form of the momentum equation in (7) with the associated subgrid stress in (8) and the subgrid energy production $\mathcal{P}$ in (11) have been analyzed by Lilly,[4] Deardorff,[5] Leonard,[3] Clark *et al.*,[6] Mansour *et al.*,[7] Antonopoulos-Domis,[8] and Rogallo and Moin.[9] Lilly[4] first proposed approximating $\overline{\bar{u}_i\bar{u}_j} \approx \bar{u}_i\bar{u}_j$ in (7), while Leonard[3] proposed explicitly evaluating the $\overline{\bar{u}_i\bar{u}_j}$ term for various simple filter functions. Clark *et al.*[6] further approximated the resolved-subgrid terms in (8) as $\overline{\bar{u}_i u_j^{sgs}} + \overline{u_i^{sgs}\bar{u}_j} \approx 0$ and modeled the subgrid-subgrid term $\overline{u_i^{sgs}u_j^{sgs}}$ with an eddy-viscosity representation. Owing to the inaccuracy of these early approximations, most subsequent large-eddy simulations have instead been based on the form of the momentum equation in (1).

More recently several studies[2,10–12] have used the momentum equation in (7) with various subgrid-scale models for large eddy simulations. The present study is also based on (7), but uses the multifractal model from Part I to represent the subgrid stress, together with an explicit filter for evaluating $\overline{\bar{u}_i\bar{u}_j}$.

C. The multifractal subgrid-scale model

The multifractal subgrid-scale model is based on a representation of the subgrid vorticity field in terms of a scale-invariant multiplicative cascade for the subgrid enstrophy, and an additive cascade for the progressively isotropic decorrelation of the subgrid vorticity orientation from the smallest resolved scale Δ. The subgrid velocities u_i^{sgs} in (8) then result from Biot–Savart integrals over this modeled subgrid vorticity field. A complete derivation of the model and the explicit filter used in evaluating τ_{ij}^* in (8) and $\overline{\bar{u}_i\bar{u}_j}$ in (7) is given in Part I. To implement the multifractal model, the momentum equation in (7) is solved with

$$\tau_{ij}^* \approx \mathcal{B}(\overline{\bar{u}_i u_j^\Delta} + \overline{\bar{u}_j u_i^\Delta}) + \mathcal{B}^2\overline{u_i^\Delta u_j^\Delta}, \tag{14}$$

where

$$\mathcal{B} \equiv 0.47\ 2^{-(2/3)\mathcal{N}}[2^{(4/3)\mathcal{N}} - 1]^{1/2} \tag{15}$$

with the number $\mathcal{N}$ of iterations in the multifractal cascade given by

$$\mathcal{N} \equiv \log_2(\Delta/\lambda_\nu). \tag{16}$$

Each of the filtered products represented by the long overbars in (14) is explicitly evaluated as

$$\overline{\bar{u}_i u_j^\Delta} \approx \frac{1}{\Delta^3}\int_{\Delta^3} \mathcal{G}_i(\mathbf{x})\mathcal{H}_j(\mathbf{x})d^3\mathbf{x}, \tag{17}$$

$$\overline{u_i^\Delta u_j^\Delta} \approx \frac{1}{\Delta^3}\int_{\Delta^3} \mathcal{H}_i(\mathbf{x})\mathcal{H}_j(\mathbf{x})d^3\mathbf{x}, \tag{18}$$

and the filtered product of the resolved velocity components in (7) is similarly evaluated as

$$\overline{\bar{u}_i\bar{u}_j} \approx \frac{1}{\Delta^3}\int_{\Delta^3} \mathcal{G}_i(\mathbf{x})\mathcal{G}_j(\mathbf{x})d^3\mathbf{x}. \tag{19}$$

The functions $\mathcal{G}_i(\mathbf{x})$ and $\mathcal{H}_i(\mathbf{x})$ in (17)–(19) are tensor-product expansions of $\bar{u}_i(\mathbf{x})$ and $u_i^\Delta(\mathbf{x})$, respectively, using Legendre basis functions Φ_k as

$$\bar{u}_i(\mathbf{x}) \approx \sum_{l,m,n} a_{lmn}\Phi_l(x)\Phi_m(y)\Phi_n(z) \equiv \mathcal{G}_i(\mathbf{x}), \tag{20}$$

$$u_i^\Delta(\mathbf{x}) \approx \sum_{l,m,n} b_{lmn}\Phi_l(x)\Phi_m(y)\Phi_n(z) \equiv \mathcal{H}_i(\mathbf{x}), \tag{21}$$

where the required cell-centered values of u_i^Δ are obtained from the cell-centered values of $\bar{u}_i(\mathbf{x})$ as

$$u_i^\Delta \equiv \bar{u}_i - a_{000}. \tag{22}$$

Equations (7) and (14)–(22) give a complete statement of the multifractal model for large-eddy simulation.

III. ENERGY TRANSFER BY THE MULTIFRACTAL MODEL

Here we assess the energy transfer implied by the multifractal subgrid-scale model given above, including the subgrid part $\mathcal{P}^*(\mathbf{x},t)$ in (12) and the resolved part $\mathcal{P}^R(\mathbf{x},t)$ in (13), as well as the combined subgrid energy transfer $\mathcal{P}(\mathbf{x},t)$ in (11). Figure 1 shows correlations of all three of these fields, obtained from 512^3 DNS velocity fields for forced homogeneous isotropic turbulence filtered onto a 32^3 grid to simulate the resolved velocity fields in a large-eddy simulation, and provided as the inputs to the multifractal subgrid-scale model. The resulting correlation coefficient of 0.85 for $\mathcal{P}^*$, which gives the contributions from $\tau_{ij}^*(\mathbf{x},t)$ to the total subgrid energy production, is consistent with the results in Part I. As noted there, at least some of the errors in $\mathcal{P}^*$ are due to correlations that result from the multifractal cascade for the subgrid vorticity field, but which were ignored in evaluating the Biot–Savart integral in Part I from the multifractal subgrid vorticity field.

It is here further apparent from the results in Fig. 1 that there is a very high correlation, exceeding 0.997, in the resolved part $\mathcal{P}^R$ that gives the contributions from $\overline{\bar{u}_i\bar{u}_j}$ to the combined subgrid energy production in (11). This indicates that the explicit filter used in (19) to evaluate $\overline{\bar{u}_i\bar{u}_j}$ is extremely accurate for the conditions considered here. Moreover, since the relative sizes of the original 512^3 DNS grid

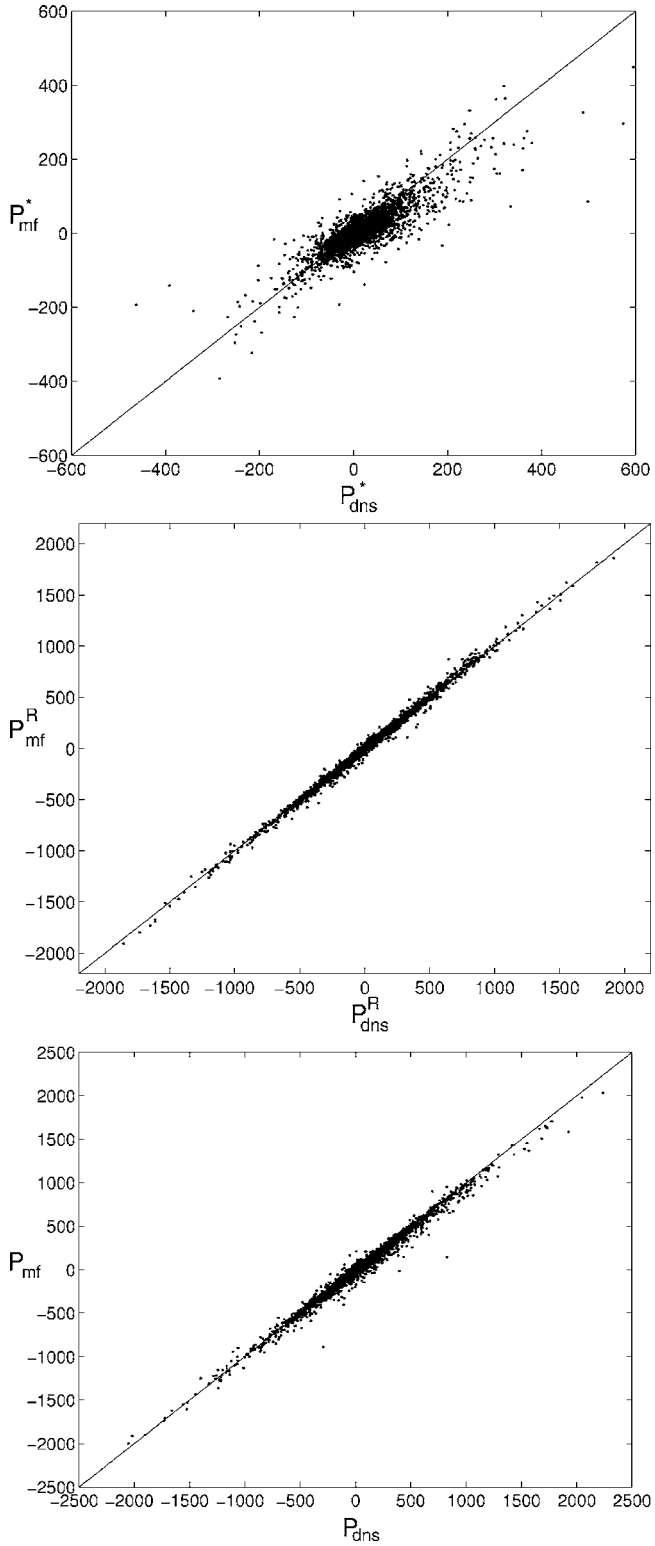

FIG. 1. Correlations for the subgrid energy production field $\mathcal{P}(\mathbf{x},t)$ from the multifractal subgrid-scale model and corresponding exact values from 512^3 DNS fields filtered onto the same 32^3 LES grid, showing results for the subgrid part $\mathcal{P}^*(\mathbf{x},t)$ (top), the resolved part $\mathcal{P}^R(\mathbf{x},t)$ (middle), and the combined total $\mathcal{P}(\mathbf{x},t)$ (bottom), giving correlation coefficients of 0.85, 0.997, and 0.99, respectively.

and the filtered 32^3 grid used to simulate the resolved velocity fields provide for significant subgrid-scale turbulence, the present high correlation should be reasonably indicative of practical LES conditions. At these conditions the resolved

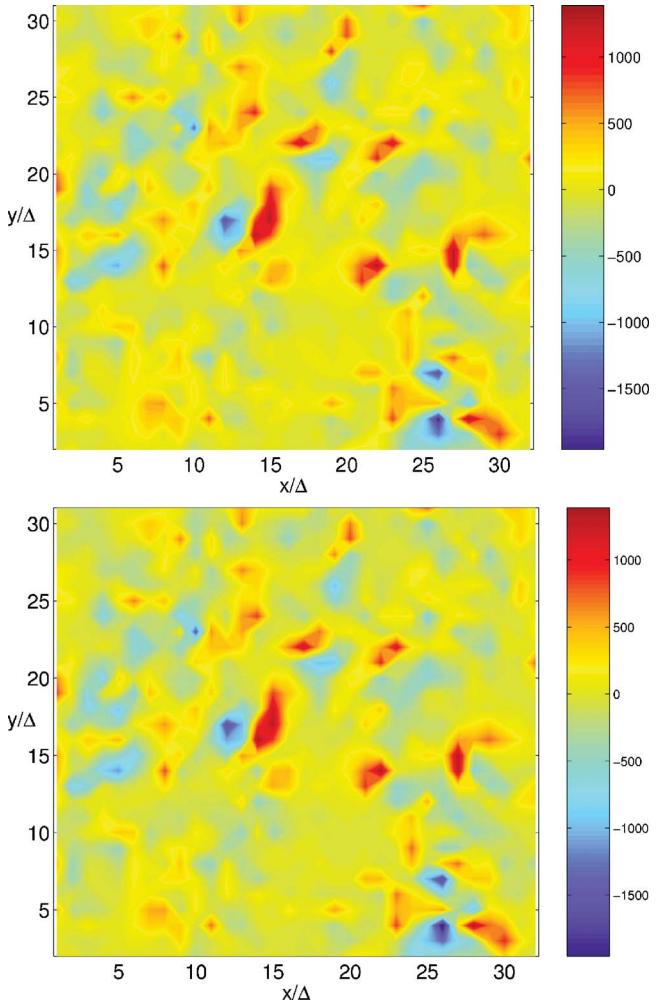

FIG. 2. (Color). Typical comparisons of two-dimensional intersections through the subgrid energy production field $\mathcal{P}(\mathbf{x},t)$ on the 32^3 LES grid, showing the result from the multifractal subgrid-scale model (top) and the corresponding exact result from the 512^3 DNS field filtered onto the same 32^3 grid (bottom). The same color scale is used for both fields to allow direct comparisons. Note local regions of large forward scatter and backscatter of energy between the resolved and subgrid scales.

part $\mathcal{P}^R$ is found to contribute more than 80% of the total subgrid energy production $\mathcal{P}$. Thus it is not surprising that the correlation in Fig. 1 between the total subgrid production $\mathcal{P}$ from the multifractal model and from the filtered DNS data is also in excess of 0.99. While it has long been understood[13] that the filter kernel strongly influences $\mathcal{P}(\mathbf{x},t)$, for smooth filters a relatively precise estimate for the lower bound of the contribution of $\mathcal{P}^R$ to $\mathcal{P}$, corresponding to arbitrarily high cell Reynolds numbers Re_Δ, is given by Leonard[3] as 0.3 ± 0.1. This suggests that even at much larger Re_Δ values typical of many practical large-eddy simulations, $\mathcal{P}^R$ will remain a substantial contributor to $\mathcal{P}$. Given the relative accuracy of the explicit filter used in (19) to evaluate $\overline{\overline{u}_i\overline{u}_j}$, this suggests that high accuracy in the total subgrid energy production $\mathcal{P}(\mathbf{x},t)$ seen in Fig. 1 will be maintained with the present model even at large Re_Δ values.

Figure 2 compares a typical two-dimensional intersection through the total subgrid energy production fields $\mathcal{P}(\mathbf{x},t)$ obtained from the multifractal model with the filtered DNS

data. It is apparent that the result in the top panel from the multifractal model gives an extremely accurate representation of the "exact" result in the bottom panel. In particular, both the forward transfer and backscatter of energy between the resolved and subgrid fields are accurately reproduced by the model. The considerations above indicate that as Re_Δ becomes arbitrarily large, some decrease in the accuracy of $\mathcal{P}(\mathbf{x},t)$ from the multifractal model may be expected, but the continued contribution of the resolved part $\mathcal{P}^R$ to the total subgrid production $\mathcal{P}$ and the relatively high accuracy of the explicit filter in evaluating $\overline{\bar{u}_i\bar{u}_j}$ indicate that the model will continue to provide an accurate representation of the subgrid production field.

IV. CONTROL OF NUMERICAL ERRORS

As noted in the Introduction, irrespective of the fidelity in $\tau_{ij}(\mathbf{x},t)$ and $\mathcal{P}(\mathbf{x},t)$ of the subgrid-scale model used in any large-eddy simulation, the calculation must additionally provide a means for controlling errors introduced by the numerics of the solver itself. Some of these errors will act to degrade the accuracy of the simulation without necessarily destabilizing it, and significant effort has been expended to understand and develop techniques for reducing such errors in large-eddy simulations.[14–17] Other errors such as aliasing can introduce spurious energy into the resolved scales which, unless removed, will destabilize the calculation. Many prior approaches have removed this spurious energy by modifying an eddy viscosity in the subgrid-scale model to provide an explicit increase in the forward transfer of energy from the resolved scales. While such approaches can ensure an appropriate average rate of subgrid energy production to give the correct overall energy in the resolved scales, the resulting subgrid-scale stress and subgrid energy production fields $\tau_{ij}(\mathbf{x},t)$ and $\mathcal{P}(\mathbf{x},t)$ typically lack significant fidelity. Aside from such purely dissipative subgrid-scale models, a number of other approaches[18–23] have explicitly allowed for backscatter to permit higher-fidelity representations for $\tau_{ij}(\mathbf{x},t)$ and $\mathcal{P}(\mathbf{x},t)$. Such backscatter can, however, lead to computational instabilities due to the additional energy being introduced in the resolved scales, and thus such approaches have limited the backscatter in various ways to stabilize the calculation. Typically this is done by modifying an eddy viscosity, though doing so generally further decreases the fidelity of the subgrid stress and energy production fields.

Unlike eddy-viscosity models, the present multifractal subgrid-scale model was shown in Sec. III to provide remarkably accurate representation of both forward transfer and backscatter of energy in $\mathcal{P}(\mathbf{x},t)$ between the resolved and subgrid scales. However, as with any model it must additionally provide a means to control the effects of numerical errors introduced by the flow solver. In this section we demonstrate how this spurious energy can be effectively controlled by means of a backscatter limiter that does not significantly reduce the fidelity in the spatial and temporal structure of the subgrid energy production field $\mathcal{P}(\mathbf{x},t)$ or the stress fields $\tau^*_{ij}(\mathbf{x},t)$ and $\overline{\bar{u}_i\bar{u}_j}(\mathbf{x},t)$.

A. Backscatter limiting for large-eddy simulations

We show here that the spurious energy introduced in the resolved scales by explicitly including backscatter may be removed by limiting the magnitude of those stresses responsible for the backscatter of energy into the resolved scales. As understood for over a decade, in actual turbulent flows energy is transferred both from the resolved to the subgrid scales as well as from the subgrid to the resolved scales, often in approximately equal proportions.[13] Thus the energy production $\mathcal{P}$ may be decomposed into terms involving forward transfer of energy where

$$\mathcal{P}^{forw.}_{(ij)}(\mathbf{x},t) \equiv -(\overline{\bar{u}_{(i)}\bar{u}_{(j)}} + \tau^*_{(ij)})^d\bar{S}_{(ij)} > 0, \tag{23}$$

with subscript parentheses indicating that no sum is implied, and backscatter of energy where

$$\mathcal{P}^{back}_{(ij)}(\mathbf{x},t) \equiv -(\overline{\bar{u}_{(i)}\bar{u}_{(j)}} + \tau^*_{(ij)})^d\bar{S}_{(ij)} < 0, \tag{24}$$

and where the superscript "d" denotes the deviatoric part of the tensor. The full energy transfer field is then given by

$$\mathcal{P}(\mathbf{x},t) = \sum_{(ij)} \mathcal{P}^{forw.}_{(ij)}(\mathbf{x},t) + \sum_{(ij)} \mathcal{P}^{back}_{(ij)}(\mathbf{x},t). \tag{25}$$

While (23)–(25) define the local energy transfer in the continuous system, in a discrete simulation backscatter may give rise to artificial amplification of resolved energy and lead to destabilization of the simulation, as discussed above. Thus the energy transfer of a discrete system $\mathcal{P}^{disc.}$ is given by

$$\mathcal{P}^{disc.}(\mathbf{x},t) \equiv \sum_{(ij)} \mathcal{P}^{forw.}_{(ij)}(\mathbf{x},t) + \sum_{(ij)} \mathcal{P}^{back}_{(ij)}(\mathbf{x},t) + \boldsymbol{\varepsilon}(\mathbf{x},t), \tag{26}$$

where $\boldsymbol{\varepsilon}$ is the erroneous backscatter to the resolved scales. Given that the numerical error should originate where resolved-scale gradients are large, and thus where the natural backscatter is also relatively large, it appears reasonable to expect this error to be proportional to the magnitude of the backscatter components of (24) and thus given by

$$\boldsymbol{\varepsilon}(\mathbf{x},t) \approx \eta \sum_{(ij)} \mathcal{P}^{back}_{(ij)}(\mathbf{x},t), \tag{27}$$

with η the constant of proportionality.

The artificial backscatter $\boldsymbol{\varepsilon}$ in (27) may be eliminated in the discrete system, however, by making small reductions in the local magnitude to those stress components that contribute to local backscatter of energy from the subgrid scales to the resolved scales. To do this, the limiter first calculates each of the terms $\mathcal{P}_{(ij)}$ from (23)–(25) that contribute to the local subgrid production. Any of the local $\mathcal{P}_{(ij)}$ terms that are negative will contribute to local backscatter of energy, and thus only those terms are reduced as

$$\widehat{\mathcal{P}_{(ij)}} \equiv (1 - C_{\mathcal{B}})\mathcal{P}_{(ij)}, \tag{28}$$

where

$$C_{\mathcal{B}} \equiv \frac{\eta}{1+\eta} \tag{29}$$

is the prescribed backscatter-limiter coefficient in terms of η in (27). This has the effect of locally reducing the contribution to backscatter into the resolved scales by the amount $C_{\mathcal{B}}\mathcal{P}_{(ij)}$, which is largest where $\mathcal{P}_{(ij)}$ is most strongly negative and thus where by (27) the numerical errors are also approximately largest.

To implement this in the momentum equation in (7), for each (ij) in (25) for which $\mathcal{P}_{(ij)}<0$ the corresponding production term $\mathcal{P}_{(ij)}$ is effectively replaced with $\widehat{\mathcal{P}_{(ij)}}$ from (28) by replacing the corresponding $(\overline{\bar{u}_{(i)}\bar{u}_{(j)}})^d$ in (7) with the backscatter-limited value

$$\left(\widehat{\overline{\bar{u}_{(i)}\bar{u}_{(j)}}}\right)^d = (1-C_{\mathcal{B}})\left(\overline{\bar{u}_{(i)}\bar{u}_{(j)}}\right)^d, \tag{30}$$

and replacing the corresponding $(\tau^*_{(ij)})^d$ in (7) with the backscatter-limited value

$$\left(\widehat{\tau^*_{(ij)}}\right)^d = (1-C_{\mathcal{B}})\left(\tau^*_{(ij)}\right)^d. \tag{31}$$

Altering the components in the momentum equation in this manner is equivalent to backscatter-limiting the subgrid energy production field $\mathcal{P}(\mathbf{x},t)$ as in (28).

The total energy transfer in the backscatter-limited computational system is then given by

$$\widehat{\mathcal{P}^{disc.}}(\mathbf{x},t) \equiv \sum_{(ij)} \mathcal{P}^{forw.}_{(ij)}(\mathbf{x},t) + (1-C_{\mathcal{B}})\sum_{(ij)} \mathcal{P}^{back}_{(ij)}(\mathbf{x},t) + (1-C_{\mathcal{B}})\boldsymbol{\varepsilon}(\mathbf{x},t). \tag{32}$$

Combining (27), (29), and (32), the reduction of the backscatter stresses gives

$$\widehat{\mathcal{P}^{disc.}}(\mathbf{x},t) = \mathcal{P}(\mathbf{x},t), \tag{33}$$

with $\mathcal{P}(\mathbf{x},t)$ given by (25), i.e., the energy transfer in the discrete computational system equals the energy transfer in the continuous system, and hence, the artificial backscatter energy has been eliminated.

It is also apparent from the considerations above that the limiter procedure could alternatively be implemented by an analogous forward-transfer accelerator procedure, in which the backscatter reduction factor $(1-C_{\mathcal{B}})$ in (28) is replaced by a forward-transfer acceleration factor $(1+C_{\mathcal{F}})$ for each (ij) in (25) for which $\mathcal{P}_{(ij)}>0$. Similarly, a mixed backscatter-limiter and forward-transfer accelerator could also be implemented. The net effect on the subgrid energy production $\mathcal{P}$ should be largely similar for all these schemes, since it is only the net $\mathcal{P}$ resulting from the sum over all the $\mathcal{P}_{(ij)}$ terms in (25) that determines the local energy transfer between the resolved and subgrid scales.

B. Effects of numerical discretization and backscatter limiting

Backscatter limiting as described here for control of numerical errors is separate from the physical model for the subgrid scales presented in this paper, and in principle can be applied to LES using any other subgrid model. It represents a new numerical method to control errors arising from a discrete under-resolved turbulence simulation that explicitly incorporates backscatter of energy into the resolved scales. The amount of these numerical errors will vary locally, and depend in part on the particulars of each discrete implementation, such as the derivative stencil, interpolation method, grid selection, and frame of reference. As such, the net amount of local backscatter limiting required to remove these errors also will depend in part upon these factors.

This may be illustrated by a simple analytical example. Let the stress tensor τ be given, using arbitrary dimensions, by

$$\tau = \begin{pmatrix} 1 & -1 \\ -1 & -1 \end{pmatrix}, \tag{34}$$

and the strain-rate tensor $\bar{S}$ be given similarly by

$$\bar{S} = \begin{pmatrix} 1 & 1 \\ 1 & -1 \end{pmatrix}. \tag{35}$$

Both tensors are symmetric and traceless. In the continuous case, the subgrid energy production implied by (34) and (35) is then given by

$$\mathcal{P} = -\tau_{ij}\bar{S}_{ij} = 1+1-1-1 = 0. \tag{36}$$

Note here that each diagonal stress component produces a contribution of "1" to the backscatter of energy into the resolved scales. In the discrete computational case, however, the energy production will include the artificial contribution $\boldsymbol{\varepsilon}$ produced by the backscatter stresses. From the results of Sec. IV C that show $C_{\mathcal{B}}\approx 0.15$, corresponding to $\eta\approx 0.18$ in (29), the energy transfer in the discrete case is given from (26), with $\boldsymbol{\varepsilon}=2(0.18)(-1)=-0.36$ from (27), by

$$\mathcal{P}^{disc.} = -\tau_{ij}\bar{S}_{ij} + \boldsymbol{\varepsilon} = 1+1-1-1-0.36 = -0.36. \tag{37}$$

Applying backscatter reduction via (32), the backscatter-limited subgrid energy production is then given by

$$\widehat{\mathcal{P}^{disc.}} = -\widehat{\tau_{ij}}\widehat{\bar{S}_{ij}} = 1+1-0.85-0.85-0.30 = 0, \tag{38}$$

which demonstrates that the backscatter reduction has eliminated the artificial backscatter of energy into the resolved scales. Thus the backscatter-limited discrete energy production $\widehat{\mathcal{P}^{disc.}}$ in (38) equals the energy production $\mathcal{P}$ of the continuous system of (36).

Let us now rotate the frame by $\pi/3$ radians, and use primes to denote quantities in the rotated frame. From (34) the rotated stress tensor τ' then becomes

$$\tau' = \begin{pmatrix} -1.366 & -0.366 \\ -0.366 & 1.366 \end{pmatrix}, \tag{39}$$

and from (35) the rotated strain-rate tensor $\overline{S'}$ becomes

$$\overline{S'} = \begin{pmatrix} 0.366 & -1.366 \\ -1.366 & -0.366 \end{pmatrix}. \tag{40}$$

The subgrid energy production in the rotated continuous case is now given by

$$\mathcal{P}' = -\tau'_{ij}\overline{S'}_{ij} = \tfrac{1}{2} + \tfrac{1}{2} - \tfrac{1}{2} - \tfrac{1}{2} = 0, \tag{41}$$

confirming that the total energy production of the continuous system is equal in the two frames, as expected. However, comparing (36) with (41), it is evident that the skew stress components in the rotated frame produce backscatter at a rate only half that of the diagonal stresses in the unrotated frame. Thus in the rotated discrete computational system, the resulting energy production is given from (26), with $\boldsymbol{\varepsilon}' = 2(0.18) \times (-1/2) = -0.18$ from (27), by

$$\mathcal{P}^{disc.\prime} = -\tau'_{ij}\overline{S'}_{ij} + \boldsymbol{\varepsilon}' = \tfrac{1}{2} + \tfrac{1}{2} - \tfrac{1}{2} - \tfrac{1}{2} - 0.18 = -0.18. \tag{42}$$

Comparing this with the analogous result in (37), it is apparent that the rotated frame produces approximately half as much false backscatter as the unrotated frame, and thus requires only half as much backscatter reduction. Indeed, from (32) the backscatter-limited subgrid energy production in the rotated frame is given by

$$\widehat{\mathcal{P}^{disc.\prime}} = -\widehat{\tau'_{ij}}\overline{S'}_{ij} = \tfrac{1}{2} + \tfrac{1}{2} - 0.43 - 0.43 - 0.15 = 0, \tag{43}$$

which confirms that the backscatter limiting eliminates the false backscatter $\boldsymbol{\varepsilon}'$ and recovers the correct energy production of the continuous field $\mathcal{P}$ in (36). Consequently, as this example demonstrates, while the amount of backscatter reduction necessarily varies in the two discrete implementations, the resulting backscatter-limited energy production is the same in both cases, and is equal to that of the continuous field, namely

$$\widehat{\mathcal{P}^{disc.\prime}} = \widehat{\mathcal{P}^{disc.}} = \mathcal{P}. \tag{44}$$

C. Evaluation of the backscatter limiter

To test this approach for controlling numerical errors, the multifractal subgrid-scale model and the backscatter limiter were implemented in a flow solver for large-eddy simulations of forced homogeneous isotropic turbulence in a spatially periodic domain. The solver was based on the filtered momentum equation in (7), using a standard pressure-correction algorithm on a uniform Cartesian mesh with primitive variables stored at staggered locations, following the method of Harlow and Welch.[24] The Poisson equation was solved using standard fast Fourier transform (FFT) methods. All spatial derivatives were evaluated with fourth-order central differencing, while time integration was performed with the third-order explicit Runge–Kutta scheme of Spalart *et al.*[25] The flow was forced in standard fashion in the spectral domain at each time step by rescaling the magnitudes of the two lowest wave forms to maintain a constant total energy in these scales.

Simulations were first conducted in which the backscatter coefficient was varied between $0 \leqslant C_{\mathcal{B}} \leqslant 1$ to determine the effects of $C_{\mathcal{B}}$ on the resolved flow scales and to identify the smallest $C_{\mathcal{B}}$ value that provides for sufficient backscatter reduction to produce stable computations. Figure 3 shows the energy spectra $E(k)$ resulting from such large-eddy simulations for several values of $C_{\mathcal{B}}$, with the corresponding $E(k)$ from filtered DNS of the same flow shown by the solid symbols for comparison. Values of $C_{\mathcal{B}} < 0.10$ were found to produce insufficient removal of spurious energy from the resolved scales to provide for stable long-time simulations. For $C_{\mathcal{B}} = 0.10$ stable simulations were obtained, but the corresponding $E(k)$ in Fig. 3 showed an excess of spurious energy remaining at the intermediate and small scales. The results show that increasing $C_{\mathcal{B}} > 0.10$ removes the excess energy in these wave modes, but also causes increasing reductions in the total energy of the resolved scales. Figure 3 shows that $C_{\mathcal{B}} \approx 0.15$ represents a reasonable optimum that provides a compromise between the competing effects of instability at significantly smaller $C_{\mathcal{B}}$ values and excessive reduction of total resolved-scale energy for significantly larger $C_{\mathcal{B}}$ values. A natural extension of the present fixed value of $C_{\mathcal{B}}$ would be to adaptively determine a local $C_{\mathcal{B}}(\mathbf{x},t)$ based on the resolved flow quantities, much as the dynamic model of Germano *et al.*[20] has been used to adaptively determine the originally fixed Smagorinsky constant.

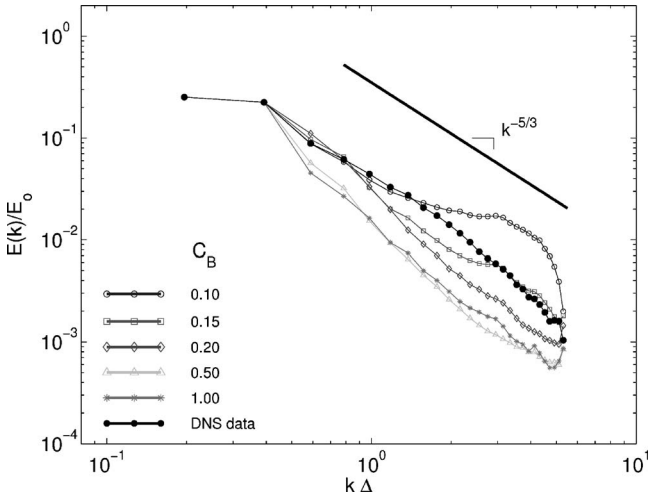

FIG. 3. Energy spectra resulting from 32^3 LES cases with the multifractal subgrid-scale model and the present backscatter limiter for various fixed values of the backscatter coefficient $C_{\mathcal{B}}$, compared with the corresponding spectrum from 512^3 DNS results filtered onto the same LES grid. The nominal value $C_{\mathcal{B}} = 0.15$ provides for sufficient reduction of aliasing effects at high wave numbers, with only moderate effects at intermediate and low wave numbers.

Figure 4 shows spectra of each of the individual stress components from such simulations, both with ($C_{\mathcal{B}} = 0.15$) and without ($C_{\mathcal{B}} = 0$) the backscatter limiter. These show that the limiter acts to reduce the stresses uniformly over the entire range of wave numbers, rather than producing changes principally at high wave numbers where most of the spurious energy is seen in Fig. 3. The dip in the spectrum at intermediate wave numbers results from the use of a fixed constant $C_{\mathcal{B}}$ in the backscatter reduction. It is this fact that causes the reduction in energy at intermediate wave numbers as $C_{\mathcal{B}}$ is successively increased to remove the spurious energy at high wave numbers.

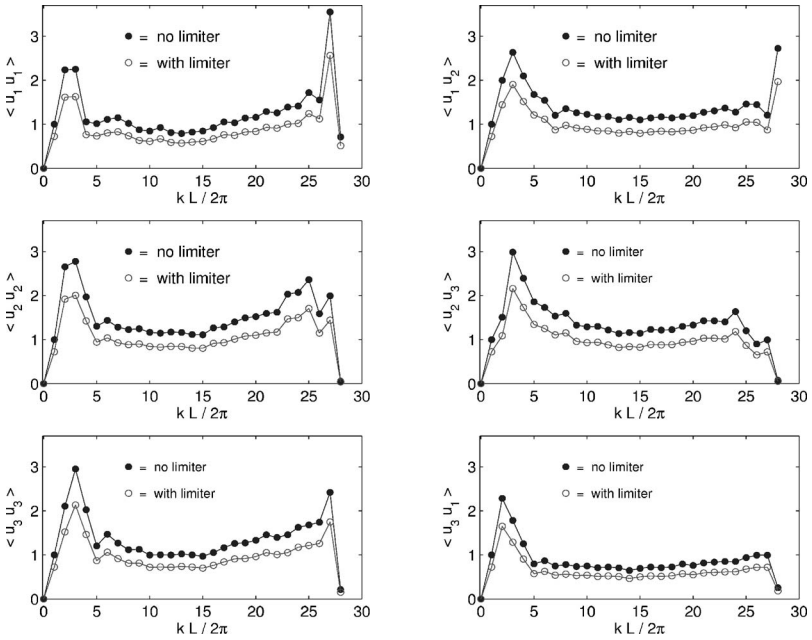

FIG. 4. Spectra of individual inertial stress components obtained from the multifractal subgrid-scale model without the backscatter limiter (solid symbols), corresponding to $C_{\mathcal{B}}=0.0$, and with the backscatter limiter (open symbols), corresponding to $C_{\mathcal{B}}=0.15$. Results verify that the present limiter acts over all wave numbers to produce the reduced energy at intermediate and low wave numbers seen for $C_{\mathcal{B}}=0.15$ in Fig. 3.

Various alternative backscatter reduction strategies were also evaluated to determine if the method described in Sec. IV A represents a reasonably optimal approach. These included a scheme with a reduction coefficient $C_{\mathcal{B}}=0.15$ but with the stress components randomly selected for limitation, rather than by the $\mathcal{P}_{(ij)}<0$ criterion noted above. At each time step approximately 45% of the components were randomly chosen for reduction (the same percentage as were reduced with the $\mathcal{P}_{(ij)}<0$ criterion) but without regard to whether the particular stress component contributed to forward transfer ($\mathcal{P}_{(ij)}>0$) or backscatter ($\mathcal{P}_{(ij)}<0$) of energy. As shown in Fig. 5, the energy spectrum $E(k)$ resulting from such random reduction shows a large deficit of energy at low wave numbers and a large excess of energy at high wave numbers that produced unstable long-time simulations. Figure 5 also shows the results obtained from leaving $\overline{\bar{u}_i\bar{u}_j}$ in (25) unchanged and limiting only the subgrid stress components $\tau^*_{(ij)}$ as in (31). For $C_{\mathcal{B}}=0.15$, and even for $C_{\mathcal{B}}=1.00$, such simulations became unstable over long-time integration, demonstrating that limiting only the subgrid-scale stresses does not provide sufficient management of resolved energy levels. Similarly, Fig. 5 also shows the effect of limiting only $\overline{\bar{u}_i\bar{u}_j}$ as in (30) with $C_{\mathcal{B}}=0.15$, while leaving τ^*_{ij} in (25) unchanged. The resulting $E(k)$ is similar to that in Fig. 3 when limiting both $\overline{\bar{u}_i\bar{u}_j}$ and τ^*_{ij}, with the principal difference being slightly more energy at high wave numbers. This is consistent with the earlier observation that roughly 80% of the total subgrid energy production $\mathcal{P}$ in these simulations is accounted for by the resolved part $\mathcal{P}^R$. Collectively, these results show that backscatter limiting of both $\overline{\bar{u}_i\bar{u}_j}$ and τ^*_{ij} as in (28)–(31) with $C_{\mathcal{B}}=0.15$ provides the most effective control of the energy introduced in the resolved field by numerical errors from the flow solver.

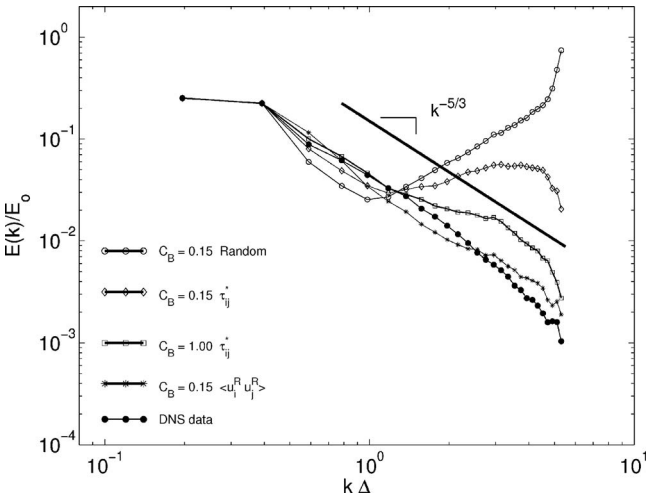

FIG. 5. Energy spectra from 32^3 LES with multifractal subgrid-scale model and backscatter limiter for various alternative limiter strategies discussed in Sec. IV C, verifying the proposed backscatter limiting of both subgrid stress and resolved stress as indicated in (30) and (31), only for (ij) values that correspond to terms $\mathcal{P}_{(ij)}>0$ in (25), which contribute to backscatter in $\mathcal{P}(\mathbf{x},t)$.

Simulations were also conducted to determine if the backscatter limiter with reduction factor $(1-C_{\mathcal{B}})$ in (28)–(31) could alternatively be implemented by an analogous forward-transfer accelerator with an enhancement factor $(1+C_{\mathcal{F}})$, or by a mixed backscatter-limiter and forward-transfer accelerator, to give a similar net reduction in the subgrid energy production $\mathcal{P}$. Figure 6 shows the resulting $E(k)$ for several combinations of backscatter reduction and forward-transfer acceleration. The reference case corresponding to $(C_{\mathcal{B}},C_{\mathcal{F}})=(0.15,0)$ from Fig. 3 is also shown for comparison, as is the filtered DNS spectrum. It is apparent that $(C_{\mathcal{B}},C_{\mathcal{F}})=(0.075,0.075)$ and $(C_{\mathcal{B}},C_{\mathcal{F}})=(0,0.15)$ produce roughly the same result as the reference case, though a small increase in the energy at the smallest resolved wave modes is evident for pure forward-transfer acceleration that did not occur for the backscatter-only limiter.

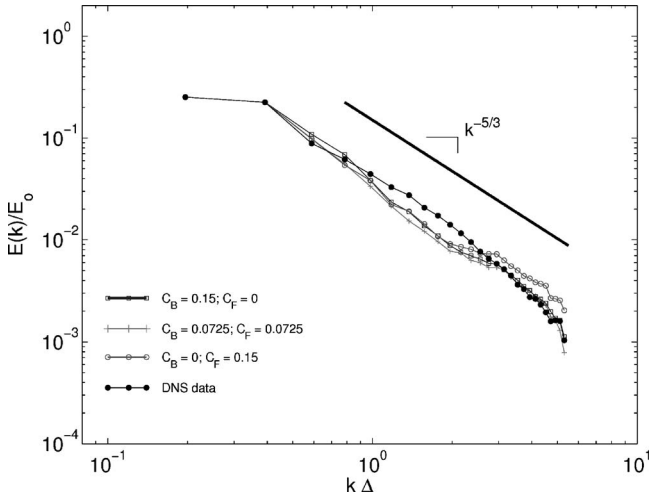

FIG. 6. Energy spectra from 32^3 LES with multifractal subgrid-scale model and various combinations of backscatter reduction with coefficient $C_{\mathcal{B}}$ and forward-scatter acceleration with coefficient $C_{\mathcal{F}}$, verifying largely similar results for the same net reduction in the subgrid energy production $\mathcal{P}$. Note slightly better results obtained for backscatter-only limiting.

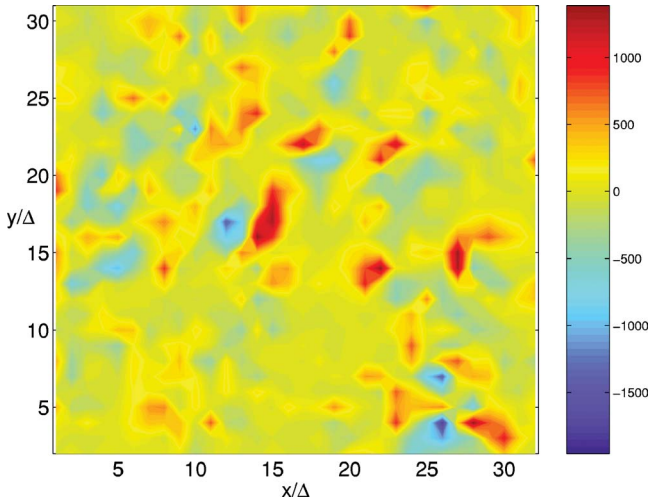

FIG. 7. (Color). Same two-dimensional intersection from the energy production field illustrated in Fig. 2, but calculated using the multifractal subgrid-scale model and a backscatter reduction coefficient $C_{\mathcal{B}}=0.15$. Comparison with DNS and nonlimited model values in Fig. 2 indicates that the operation of the backscatter limiter does not significantly affect the accuracy of the limited energy production field $\widehat{\mathcal{P}(\mathbf{x},t)}$.

D. Effect of the backscatter limiter on model performance

The effect of the backscatter limiter with $(C_{\mathcal{B}},C_{\mathcal{F}})=(0.15,0)$ on the accuracy of the multifractal subgrid-scale model was determined in tests that compared model values for the stress components and the subgrid energy production against corresponding filtered DNS results. The original 512^3 DNS velocity fields were first spatially filtered onto a 32^3 grid to provide resolved velocities that served as inputs to the subgrid model. The multifractal subgrid-scale model then predicted stress component fields $\tau_{ij}^*(\mathbf{x},t)$ and $\overline{\bar{u}_i\bar{u}_j}(\mathbf{x},t)$ and the subgrid energy production field $\mathcal{P}(\mathbf{x},t)$, first without any backscatter limiting $(C_{\mathcal{B}}=0)$ and then again with the backscatter constant at the nominal value $(C_{\mathcal{B}}=0.15)$. Figure 7 shows the subgrid energy production field $\mathcal{P}(\mathbf{x},t)$, including the backscatter limiter with $C_{\mathcal{B}}=0.15$, in the same two-dimensional intersection and with the same color scale as for $C_{\mathcal{B}}=0.15$ in Fig. 2. It is apparent by comparing with Fig. 2 that the change in the detailed spatial structure of $\mathcal{P}(\mathbf{x},t)$ due to the backscatter limiter is exceedingly small. Table I gives the resulting correlations between model values and filtered DNS values for the normal and shear stress components of $\overline{\bar{u}_i\bar{u}_j}$ and τ_{ij}^*, as well as for $\mathcal{P}^R$, $\mathcal{P}^*$, and the combined subgrid energy production $\mathcal{P}$. It is apparent from these results that, in contrast to earlier efforts[26] to limit backscatter which reported significant degradation in accuracy, use of the present backscatter limiter with the multifractal subgrid-scale model produces virtually no reduction in the accuracy seen in the $\mathcal{P}(\mathbf{x},t)$ field in Figs. 1 and 2 and in Part I.

V. *A POSTERIORI* TESTS OF THE MULTIFRACTAL MODEL: STATIONARY CASE

To determine the stability and evaluate the accuracy of the multifractal subgrid-scale model with the backscatter limiter in actual large-eddy simulations, a series of *a posteriori* tests were conducted based on LES of forced, homogeneous, isotropic turbulence in a spatially periodic domain. These tests were conducted with the same flow solver described in Sec. IV B on a 32^3 grid for values of the cell Reynolds number Re_Δ ranging from $160\leqslant Re_\Delta\leqslant 10^6$. The latter value is clearly high enough that any further increase will not produce any changes in the resolved scales. These simulations were conducted both to verify that stable long-time integrations are feasible with the multifractal model and the backscatter limiter at these Reynolds numbers, and to assess how closely the resulting resolved velocity fields from these large-eddy simulations reproduce various aspects of the structure and dynamics of high Reynolds number turbulence. These large-eddy simulations were initialized with DNS velocity fields for forced, homogeneous, isotropic turbulence on a 512^3 grid that had been filtered onto the same 32^3 LES grid. All these simulations were conducted with the backscatter limiter coefficients set to the nominal values $(C_{\mathcal{B}},C_{\mathcal{F}})=(0.15,0)$ from Sec. IV C. For the lowest Re_Δ simulation, the viscosity ν was the same as in the DNS data, allowing

TABLE I. Comparisons with and without backscatter limiter of correlation for 32^3 LES with multifractal model at $Re_\Delta\approx 160$ and corresponding DNS results filtered onto same grid, for various fields contributing to total subgrid energy production field $\mathcal{P}(\mathbf{x},t)$.

	ρ	
Statistic	Without limiter	With limiter
$(\overline{\bar{u}_i\bar{u}_j})_{normal}$	0.9980	0.9962
$(\overline{\bar{u}_i\bar{u}_j})_{shear}$	0.9981	0.9959
τ^*_{normal}	0.8600	0.8608
τ^*_{shear}	0.8608	0.8611
$\mathcal{P}^R$	0.9970	0.9949
$\mathcal{P}^*$	0.8518	0.8570
$\mathcal{P}$	0.9945	0.9914

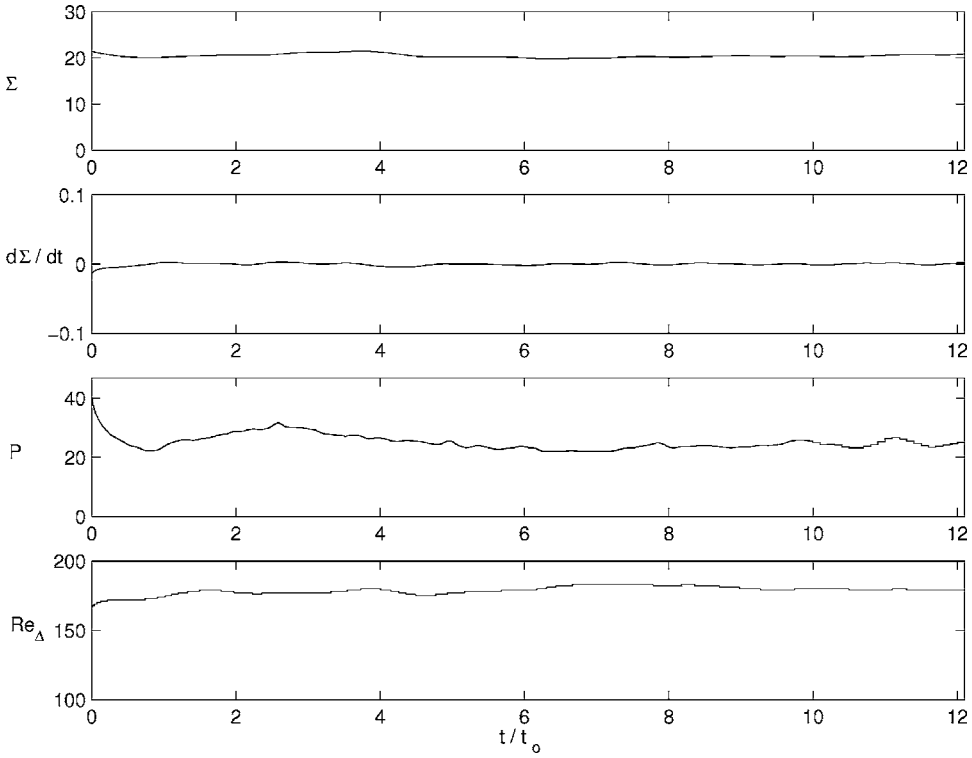

FIG. 8. Time-evolution of resolved-scale flow quantities from long-time 32^3 LES at $Re_\Delta \approx 160$ for multifractal subgrid-scale model and backscatter limiter with $C_B = 0.15$. Simulation reaches statistically stationary state after initial transient in which flow-solver and limiter adjust to imposed initial condition.

direct comparisons with the filtered DNS data after long-time LES calculations of the resolved velocity fields $\bar{u}_i(\mathbf{x},t)$.

Such comparisons with filtered DNS data are of central interest in evaluating the efficacy of any LES modeling approach. As long as the scales from the full velocity field $\mathbf{u}$ that are of interest to a particular application, are preserved in the flow simulation, the resolved velocity field $\bar{\mathbf{u}}$ and statistics associated with it, such as resolved velocity gradients $\partial\bar{u}_i/\partial x_j$, retain a clear physical meaning and hence relevance for the practicing engineer or scientist. Statistics of the subgrid field, such as the subgrid contribution to the total kinetic energy, are quantities not traditionally sought from LES, even though they may be important to certain applications, and will not be highlighted in the following evaluation.

A. Integrated quantities

For the $Re_\Delta = 160$ case, Fig. 8 shows the resulting time-evolution of the total kinetic energy Σ in the resolved scales over the entire domain, the rate of change $d\Sigma/dt$, the total subgrid energy production $\mathcal{P}$ over the entire domain, and the resulting cell Reynolds number $Re_\Delta \equiv (2\Sigma)^{1/2}\Delta/\nu$. Analogous results are shown in Fig. 9 for the highest cell-Reynolds number case, corresponding to $Re_\Delta \approx 10^6$. In both cases an initial transient is apparent in the first eddy-turnover time t_o during which the flow solver and the limiter adjust to the imposed initial conditions. Both Figs. 8 and 9 show the approach to a statistically stationary state over about one eddy-turnover time t_o, after which the energy Σ and its rate of change $d\Sigma/dt$ demonstrate stable long-time simulations as a result of the subgrid energy transfer $\mathcal{P}(\mathbf{x},t)$ produced by the multifractal subgrid model and the backscatter limiter. In addition, the simulations at both these Re_Δ values show slight time-variations in several integrated flow characteristics, particularly in the total subgrid energy transfer $\mathcal{P}$. These time-variations, however, remain stable and maintain a roughly constant amplitude and frequency throughout the simulations, suggesting that they reflect actual time-variations in the energy transfer between the resolved scales and the subgrid-scale turbulence. Similar characteristics and stability were found for the simulations at the two intermediate Re_Δ values.

B. Energy spectra

The resulting energy spectra $E(k)$ from all four cases, corresponding to $160 \leqslant Re_\Delta \leqslant 10^6$ are shown in Fig. 10. As expected for these relatively large cell Reynolds numbers, all four cases produce nearly identical energy spectra that follow the $k^{-5/3}$ inertial-range scaling. The deviations from this scaling are consistent with the effect of the backscatter limiter seen in Figs. 3 and 4. At these Reynolds numbers, the viscous dissipation $\mathcal{D}$ does not contribute significantly to the drain of energy from the resolved scales, and the flow solver must rely almost entirely on the stresses $\overline{\bar{u}_i\bar{u}_j}$ and τ_{ij}^* in $\mathcal{P}(\mathbf{x},t)$ to transfer energy to and from the resolved field. The energy transfer is thus essentially unaffected by further reduction in the viscosity, which merely reduces the inner (viscous) scale λ_ν deep within the subgrid-scale turbulence.

C. Probability densities of velocity gradients

The accuracy of these large-eddy simulations was further evaluated by examining probability densities of the velocity gradient components $\partial\bar{u}_i/\partial x_j$. Owing to the Re_Δ-independence of the resolved scales demonstrated in Fig. 10, these probability distributions will be essentially the same

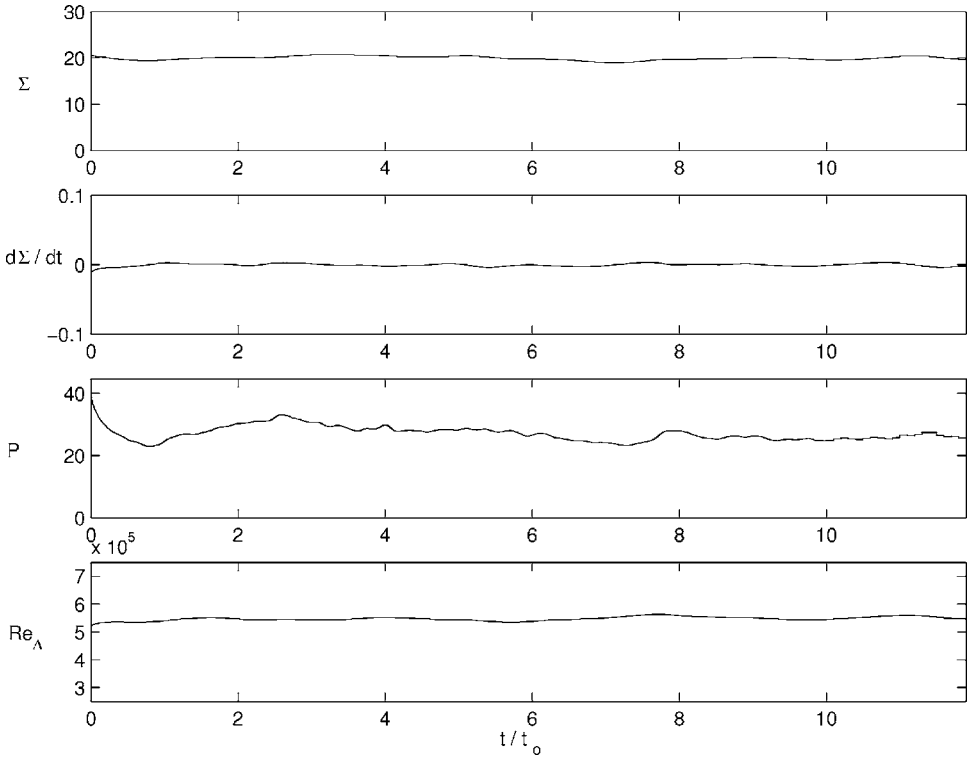

FIG. 9. Time-evolution of resolved-scale flow quantities demonstrating stable long-time 32^3 LES at $Re_\Delta \approx 10^6$ for multifractal model and backscatter limiter with $C_B=0.15$. The simulation again reaches statistically stationary state after initial transient. Further increases in Re_Δ are unlikely to produce significant changes in energetics of resolved scales.

for all four Re_Δ cases. The distributions for the $Re_\Delta \approx 160$ case were therefore compared with the corresponding filtered DNS results. Figure 11 shows the resulting comparisons for all nine velocity gradients $\partial \bar{u}_i / \partial x_j$, with the model and DNS results given, respectively, by the dashed and solid lines. The $Re_\Delta \approx 160$ value is sufficiently large to produce significant departures from Gaussian statistics due to internal intermittency in the resolved scales. This corresponds to the exponential scaling at large gradient magnitudes that is identifiable by the straight-line tails of these distributions in the semi-logarithmic axes shown in Fig. 11. It is apparent that the model results, for both the on- and off-diagonal components of the velocity gradients, are in good agreement with the distributions obtained from the filtered DNS fields. It is especially noteworthy that the multifractal subgrid-scale model accurately predicts the probability of even comparatively rare large-gradient features of the flow, some of which occur with a frequency three orders of magnitude lower than the mean.

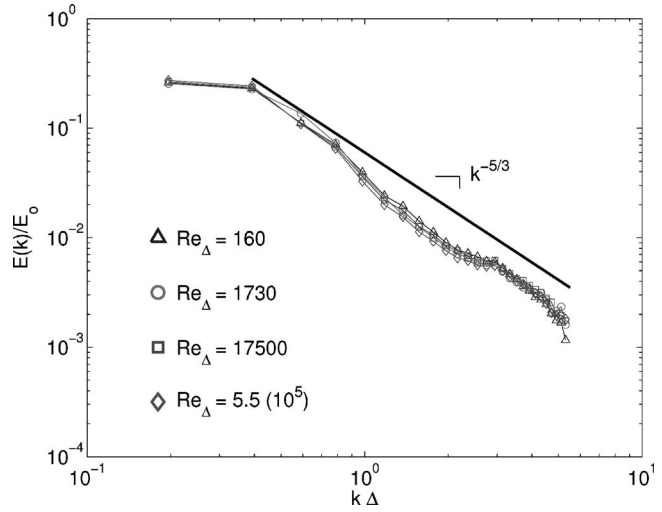

FIG. 10. Energy spectra from long time-integrations of 32^3 LES at successively increasing cell Reynolds numbers $160 \leqslant Re_\Delta \leqslant 10^6$, from multifractal model and backscatter limiter with $C_B=0.15$, verifying essentially Reynolds-number independent energetics in resolved scales at these Re_Δ values.

It is also apparent in Fig. 11 that the LES results recover the negative skewness in the on-diagonal components of the velocity gradient, as well as the much lower skewness in the off-diagonal components. This can be verified in Table II, where the variance σ^2, the skewness $\mathcal{S}_3$, and the kurtosis $\mathcal{K}_4$ values obtained from the model are shown. Table III further compares the model results with the corresponding DNS results. The average variance σ^2 of the three on-diagonal components and the six off-diagonal components of the velocity gradient fields from the model are both within 6% of the values from the filtered DNS values, with at least some of even this small difference being attributable to limits of statistical uncertainty that result from the fact that these values are obtained from statistics over the 32^3 LES grid at a single instant of time ($t/t_o \approx 12$). Moreover, in Table III the ratio of the rms values of the on- and off-diagonal velocity gradient components can be seen to be within about 5% of the $\sqrt{2}$ value for homogeneous isotropic turbulence, with at least some of this small difference again being due to the statistical uncertainty limits. Similarly, the average skewness value $\mathcal{S}_3$ of the on-diagonal velocity gradients can be seen to be within 3% of the corresponding DNS value. There are larger differences in the kurtosis values, but these increasingly higher-order moments of the velocity gradient distributions necessarily have correspondingly larger statistical uncertain-

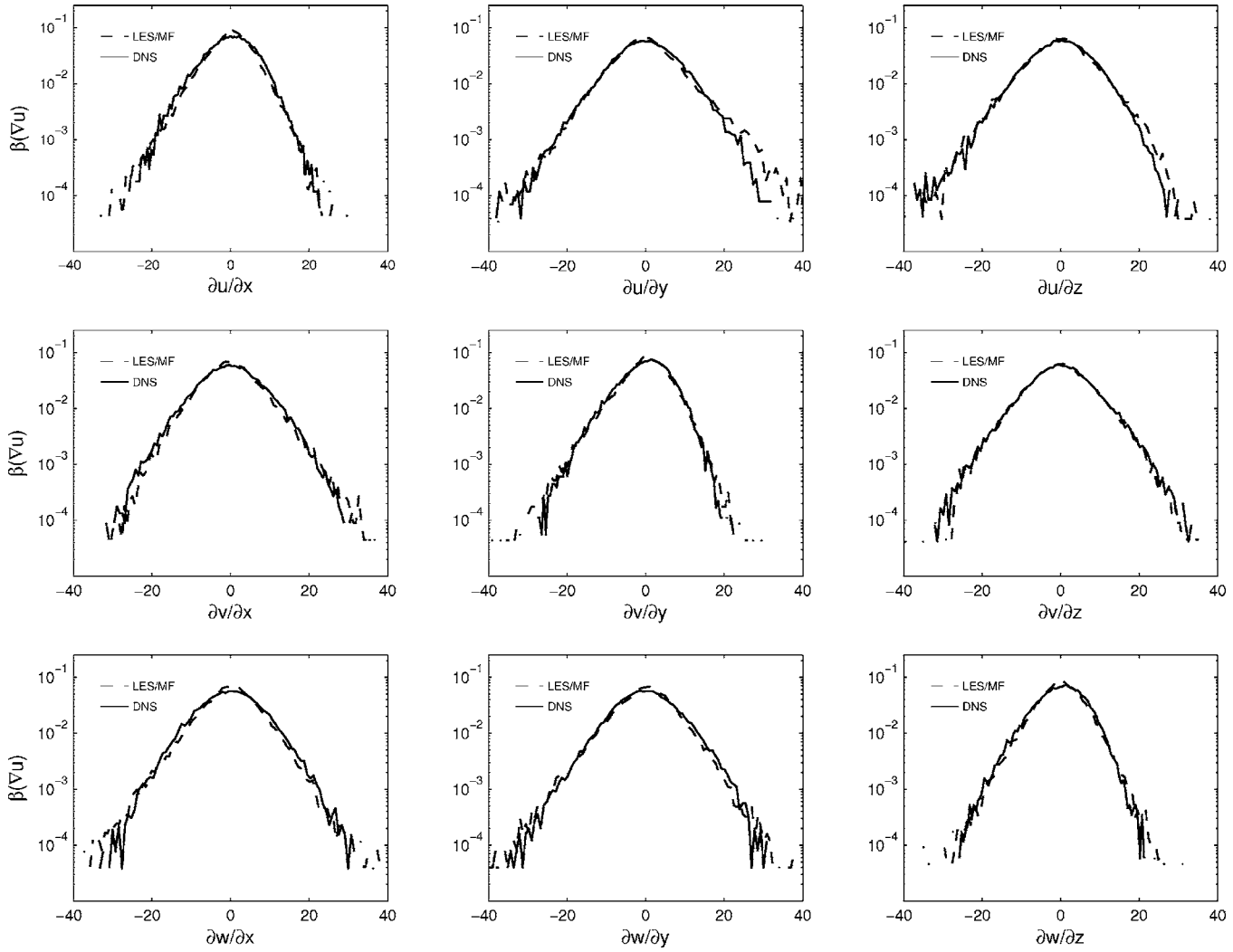

FIG. 11. Comparisons of 32^3 LES at $Re_\Delta \approx 160$ with DNS results filtered onto same grid, showing probability densities of all nine components of the resolved velocity gradients $\partial \bar{u}_i / \partial x_j$ obtained at $(t/t_o) \approx 12$ from long time-integrations with multifractal model and backscatter limiter with $C_\mathcal{B}=0.15$. Note excellent agreement of LES/MF model results (dashed line) with filtered DNS (solid line), despite strongly non-Gaussian statistics. Corresponding moments are compared in Tables II and III.

ties associated with them. In general, the distributions in Fig. 11 and the moments in Tables II and III show remarkably good agreement between the model values and the corresponding DNS values.

TABLE II. Moments of resolved velocity gradient distributions in Fig. 11 from 32^3 LES results for forced homogeneous isotropic turbulence using multifractal model at $Re_\Delta \approx 160$, showing variance σ^2, skewness $\mathcal{S}_3$, and kurtosis $\mathcal{K}_4$.

Statistic	σ^2	$\mathcal{S}_3$	$\mathcal{K}_4$
$\partial u/\partial x$	49.65	−0.346	5.951
$\partial v/\partial y$	55.38	−0.578	6.060
$\partial w/\partial z$	51.96	−0.255	5.672
$\partial u/\partial y$	101.38	0.273	5.909
$\partial u/\partial z$	98.15	−0.083	5.214
$\partial v/\partial x$	85.79	0.187	6.007
$\partial v/\partial z$	95.96	0.067	4.672
$\partial w/\partial x$	85.98	−0.135	6.336
$\partial w/\partial y$	96.76	−0.157	5.705

D. Probability densities of stress components

Similar comparisons of the probability densities for all six stress component values $\bar{u}_i \bar{u}_j$ are shown in Fig. 12, with the model and DNS results again given, respectively, by the dashed and solid lines. Generally excellent agreement is seen in both the on- and off-diagonal components of these stresses, including accurate predictions by the model of

TABLE III. Comparisons of average variance σ^2, skewness $\mathcal{S}_3$, and kurtosis $\mathcal{K}_4$ for on- and off-diagonal components of resolved velocity gradient distributions in Fig. 11 from 32^3 LES of forced homogeneous isotropic turbulence obtained with the multifractal model at $Re_\Delta \approx 160$ and DNS results filtered onto same grid, with differences approaching the limits of statistical uncertainty.

Statistic	σ^2	$\mathcal{S}_3$	$\mathcal{K}_4$
$(\partial u/\partial x)_{LES}$	52.332	−0.393	5.894
$(\partial u/\partial x)_{DNS}$	55.450	−0.406	3.713
$(\partial u/\partial y)_{LES}$	94.004	0.025	5.641
$(\partial u/\partial y)_{DNS}$	100.073	−0.042	4.108

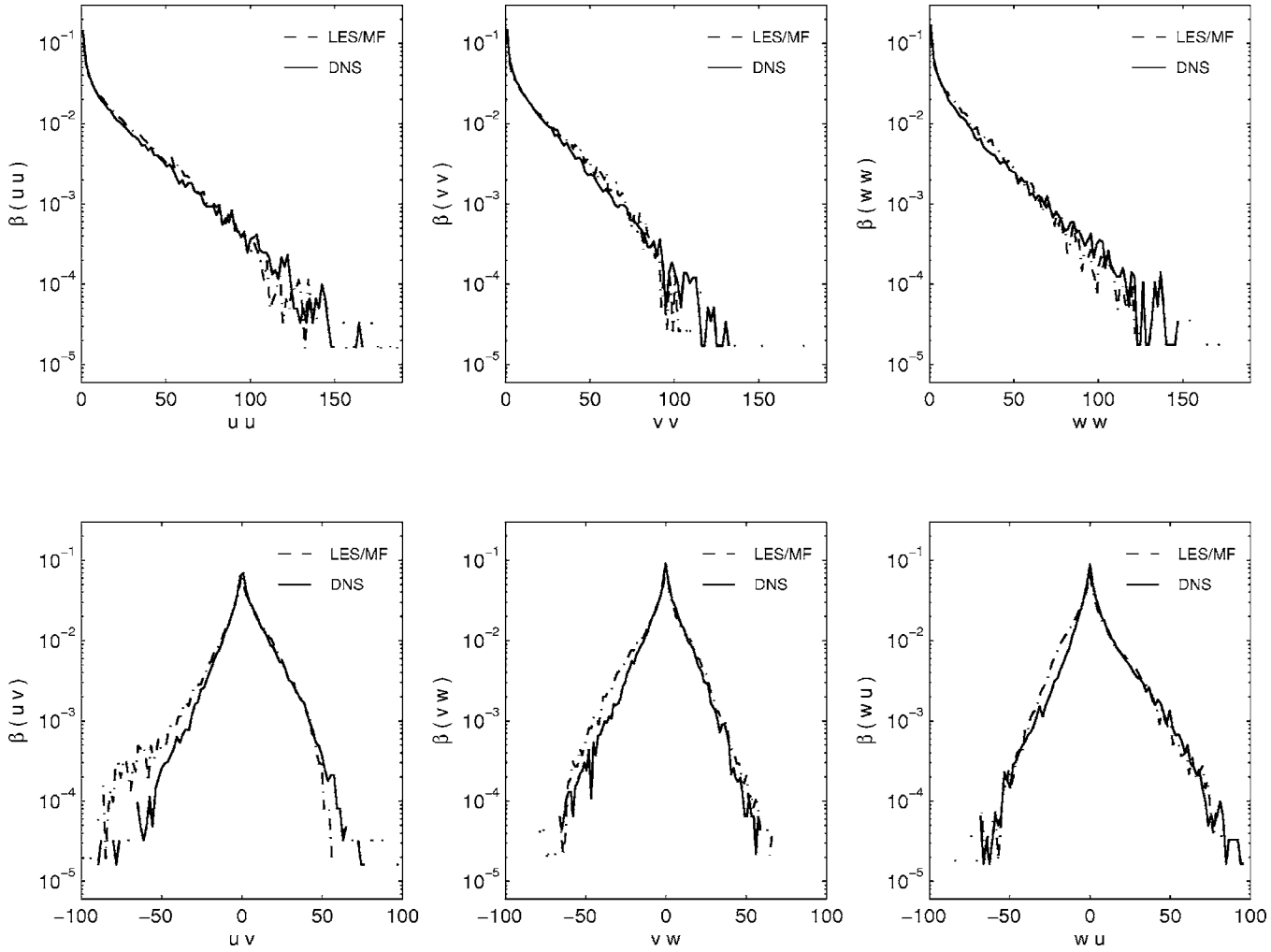

FIG. 12. Similar to Fig. 11 but comparing probability densities of six inertial stress components at $(t/t_o)\approx 12$ from 32^3 LES at $Re_\Delta \approx 160$ with DNS filtered onto same grid.

events having frequencies-of-occurrence three to four orders of magnitude lower than the mean. Figure 13 additionally shows corresponding probability densities of the viscous dissipation rate $\mathcal{D}$ and the enstrophy in the resolved scales of the flow, with the model and filtered DNS results again given, respectively, by the dashed and solid lines. It is apparent for both of these quantities that the model and DNS results are in good agreement.

VI. *A POSTERIORI* TESTS OF THE MULTIFRACTAL MODEL: DECAYING CASE

To further evaluate the accuracy of the multifractal subgrid-scale model and the backscatter limiter in large-eddy simulations, another series of *a posteriori* tests was conducted, in this case involving LES of decaying, homogeneous, isotropic turbulence. These tests extend the results in the previous section for stationary, homogeneous, isotropic turbulence by examining the ability of the multifractal subgrid model in Part I, as well as the backscatter limiter for numerical error control in Sec. IV, to adapt to changing subgrid turbulence conditions over the course of the simulation.

A. Effects of varying subgrid conditions

The present *a posteriori* tests are similar to those conducted by Hughes *et al.*[27] to evaluate the Smagorinsky model, the dynamic Smagorinsky model, and their variational multiscale method; this permits comparisons with their results obtained for those subgrid-scale models. The tests were based on 256^3 DNS of decaying, homogeneous, isotropic turbulence with initial $Re_\lambda \approx 90$ and final $Re_\lambda \approx 61$. Following Ref. 27, the DNS was first forced during $0 < t/t_o \leqslant 4.16$ to provide an initial field of stationary, homogeneous, isotropic turbulence. For $t/t_o > 4.16$ the forcing was stopped and the simulation continued through $t/t_o \approx 13$ to provide DNS of decaying, homogeneous, isotropic turbulence. The DNS field at the initial decay time $t/t_o = 4.16$ was also filtered onto a 64^3 LES grid. A large-eddy simulation with the multifractal subgrid-scale model and the backscatter limiter was then carried out over the same $4.16 < t/t_o < 13$ decay period, allowing direct comparison of the flow characteristics with the decaying DNS results filtered onto the same LES grid.

The resulting decay of the kinetic energy in the subgrid

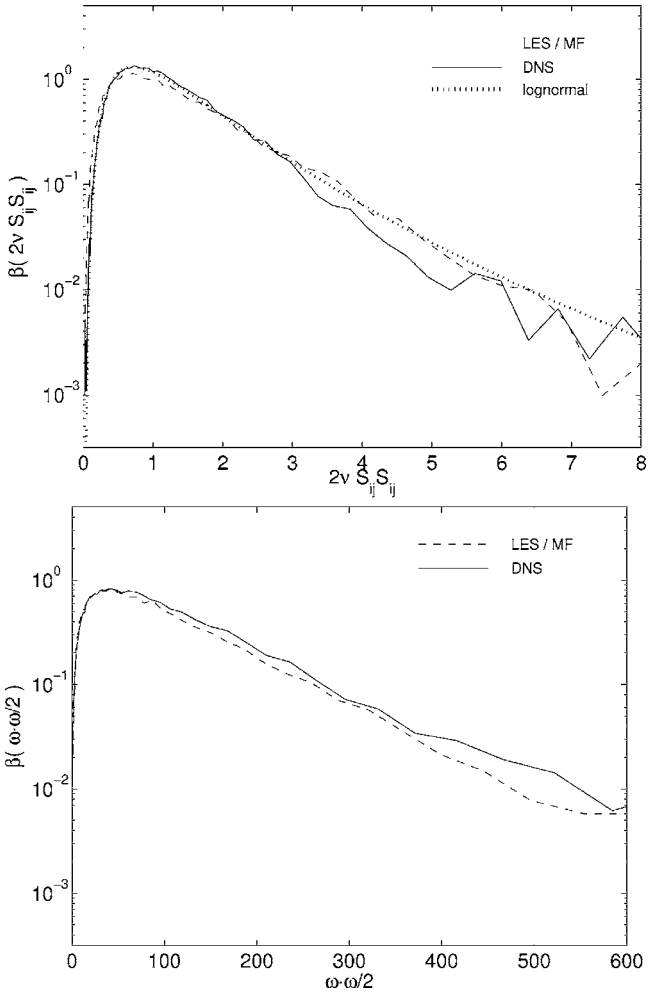

FIG. 13. Comparisons of probability densities for viscous dissipation rate (top) and enstrophy (bottom) in resolved scales at $(t/t_o)\approx 12$ from 32^3 LES at $Re_\Delta \approx 160$ and DNS results filtered onto same grid.

velocity field, together with the relatively low initial grid-scale Reynolds number Re_Δ, leads to relatively large changes in the subgrid characteristics over the course of the tests. This creates a particularly challenging case for LES, since both the subgrid-scale model and the method used to control numerical error in the simulation must adapt to these changes. In particular, the dissipation rate in the DNS results decreases by a factor of 12 over the $4.16 < t/t_o < 13$ time span of the tests, and as a result the viscous scale λ_ν in Part I increases by a factor of 1.8. Moreover, since the initial condition for the LES was obtained by filtering the 256^3 DNS field to a 64^3 LES grid, from (16) there are at most $\mathcal{N}\approx 2$ steps in the subgrid cascade at the initial time $t/t_o = 4.16$, and only about $\mathcal{N}\approx 1$ steps at the final time $t/t_o \approx 13$. This alone would lead to a significant decrease in $\mathcal{B}$ in (15), from 0.43 to 0.36, over the course of the simulation. By comparison, for the stationary case in Sec. V, in which a 512^3 DNS field was filtered onto a 32^3 LES grid, (16) indicates $\mathcal{N}\approx 4$ steps in the cascade, for which (15) gives $\mathcal{B}\approx 0.47$. The smaller initial $\mathcal{B}$ value in the present decaying case, as well as the further reduction in $\mathcal{B}$ over the course of the simulation, reflects the significantly lower levels of kinetic energy in the subgrid field.

Additionally, the result in (15) for $\mathcal{B}$ was obtained in Part I for an LES grid scale Δ in the inertial range, so that the subgrid field is dominated by inertial-range scalings. In this decaying case, following Hughes *et al.*,[27] the 256^3 DNS field was filtered onto a 64^3 LES grid, and thus Δ is in the cross-over between the inertial and dissipative ranges. As a result, the factor 0.47 in (15) for $\mathcal{B}$ must be reduced to 0.12 to reflect the lower total subgrid enstrophy $\mathcal{Q}_{sgs}$ in Part I over the corresponding inertial range value. The higher initial resolution of the 64^3 LES in this decaying case, relative to the 32^3 LES in Sec. V, also leads to half as many wave modes being aliased into the resolved scales by the flow solver. To reflect this reduced level of aliasing, the backscatter constant $C_\mathcal{B}$ must be correspondingly reduced by half, from 0.15 to 0.075. The LES resolution increases even further over the course of the decaying simulation, due to the reduction in subgrid energy, and this leads to a further reduction in the number of wave modes being aliased into the resolved scales. Accordingly, $C_\mathcal{B}$ must decrease over the course of the simulation to reflect the increasing resolution. Since $\mathcal{B}$ in (15) reflects the decrease in the total energy in the subgrid field, taking $C_\mathcal{B}(t) \sim \mathcal{B}(t)$ appropriately decreases the amount of backscatter limiting needed to control the decreasing numerical error as the resolution increases.

B. Results from LES of decaying turbulence

The total kinetic energy $\Sigma(t)$ in the resolved scales from the resulting LES simulation of decaying, homogeneous, isotropic turbulence is shown in Fig. 14. It is apparent in the top panel in Fig. 14 that the simulation accurately determines the energy decay with time. Moreover, the bottom panel in Fig. 14 compares the corresponding results from Ref. 27 for the original and dynamic versions of the Smagorinsky model with the present results from the multifractal model with the backscatter limiter. It can be seen that the errors in the present results relative to the filtered DNS are only about 1/10 as large as those from the original Smagorinsky model, and are about 1/4 as large as those resulting from the dynamic model.

Figure 15 shows the energy spectra $E(k)$ in the resolved scales at four different times in the simulation, obtained from the present LES with the multifractal subgrid model. The spectra show an inertial range with an overall reduction in the total kinetic energy. These spectra may be compared with corresponding experimentally measured spectra in active-grid-generated decaying turbulence, at much higher Reynolds number, by Kang, Chester, and Meneveau;[28] the four times shown in Fig. 15 have been chosen to match the relative energy levels at the four downstream locations in their experiments. Figure 16 additionally compares the energy spectrum in the resolved scales at $t/t_o = 6.47$ from the present LES with the result from the filtered DNS at the same time. The relatively lower energy levels at intermediate wave numbers noted in Fig. 6 are evident; roughly similar features can be seen in the corresponding results for the Smagorinsky and dynamic Smagorinsky models in Fig. 7 of Hughes *et al.*[27]

Figure 17 shows results for the decay in the total energy dissipation, including the subgrid energy production $\mathcal{P}(\mathbf{x},t)$

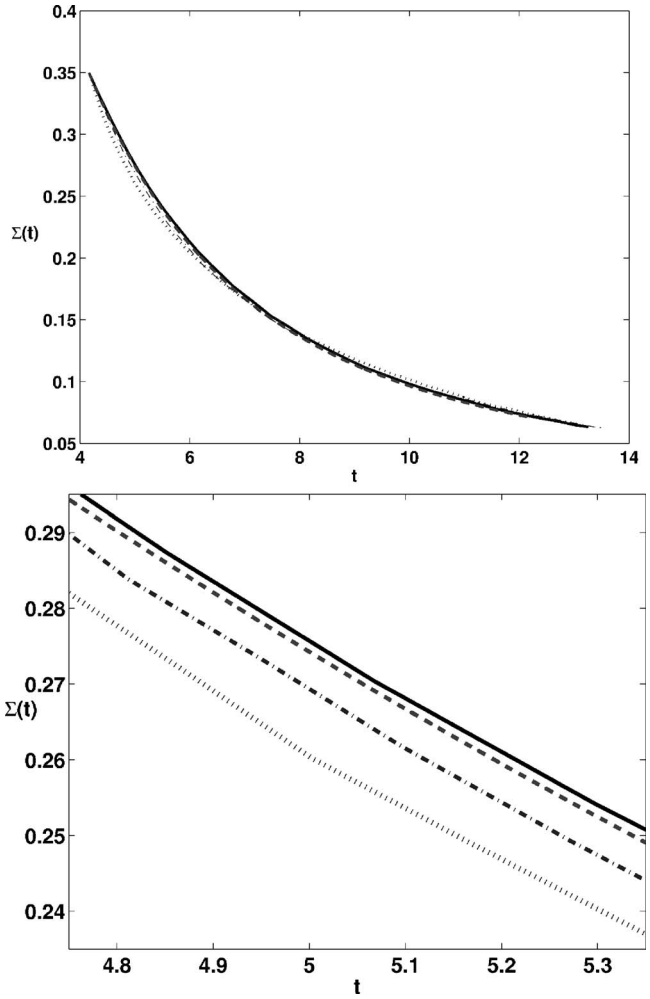

FIG. 14. Total resolved kinetic energy from decaying test case in Sec. VI, comparing filtered DNS result (solid) with LES results using multifractal subgrid-scale model (dashed), dynamic Smagorinsky model (dashed-dotted) and conventional Smagorinsky model (dotted). Shown are energy over entire simulation (top) and detail at intermediate stage (bottom), with errors from multifractal model approximately 1/10 as large as from Smagorinsky model and 1/4 as large as from dynamic model.

as well as the resolved-scale viscous dissipation $\mathcal{D}(\mathbf{x},t)$ from (4). It is apparent that the present results track the DNS decay reasonably well. Also shown for comparison are the corresponding results for the Smagorinsky and dynamic Smagorinsky models from Fig. 11 of Ref. 27. The LES results from the three SGS models are compared with the DNS result during the initial period of decay in the top panel of Fig. 18, as each of the LES simulations adjust from the imposed initial conditions, as well as at intermediate times during the decay in the bottom panel in Fig. 18. It is evident that the present results for $\mathcal{P}(\mathbf{x},t)$ rapidly adjust from the imposed initial condition to the proper value of the subgrid energy transfer, and then follow the DNS results closely thereafter.

While both the present multifractal model and the dynamic Smagorinsky model can be seen in Fig. 17 to perform reasonably well in terms of the integrated energy transfer from the resolved scales, there are fundamental differences between the two models in their ability to accurately represent the subgrid energy production field $\mathcal{P}(\mathbf{x},t)$. This can be

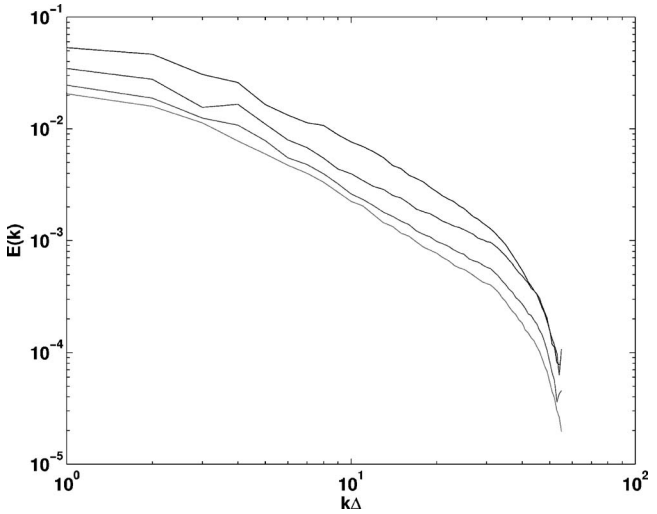

FIG. 15. Evolution of the resolved-scale energy spectrum $E(k)$ from LES with multifractal subgrid-scale model for decaying test case in Sec. VI. Times shown are at t/t_o=4.66, 6.67 8.50, and 9.65 to match relative energy levels at the four downstream locations reported in Kang *et al.* (2003).

seen in Fig. 19, which illustrates the distribution of subgrid energy production values $\mathcal{P}(\mathbf{x},t)$ taken from filtered DNS data (solid), and compares it with the dynamic Smagorinsky estimate (dashed-dotted) and that of the multifractal model (dashed). The dynamic Smagorinsky model recovers almost none of the true distribution of forward transfer and backscatter of energy of the actual turbulent flow, and only captures the net positive transfer of energy to the subgrid scales. By contrast, it is apparent that the multifractal model captures most of the distribution of forward and backscatter of energy, with the distribution of the multifractal $\mathcal{P}(\mathbf{x},t)$ differing from the DNS values by only a few percent.

The multifractal model also captures the detailed spatial structure of the energy transfer field $\mathcal{P}(\mathbf{x},t)$. This can be seen by comparing the top panel in Fig. 20, which shows $\mathcal{P}(\mathbf{x},t)$

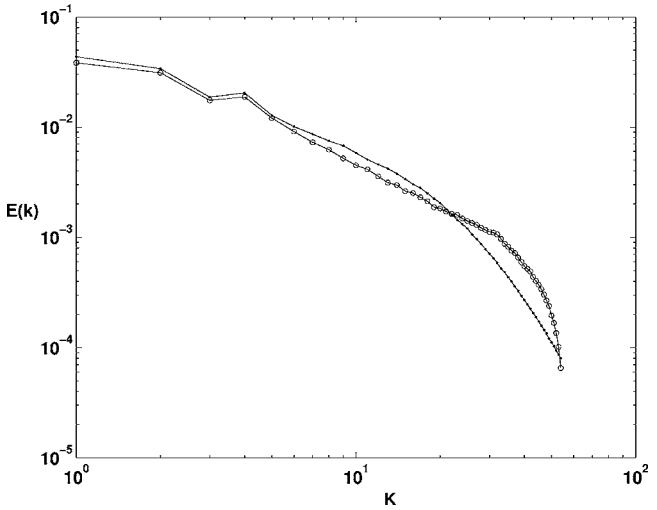

FIG. 16. Energy spectra at t/t_o=6.47 from LES with multifractal subgrid-scale model (circles) compared with filtered DNS of Hughes *et al.* (2001) (dots), showing similar energy deficit in intermediate wave modes and excess in high wave modes as seen in Fig. 6 due to fixed backscatter reduction factor C_B.

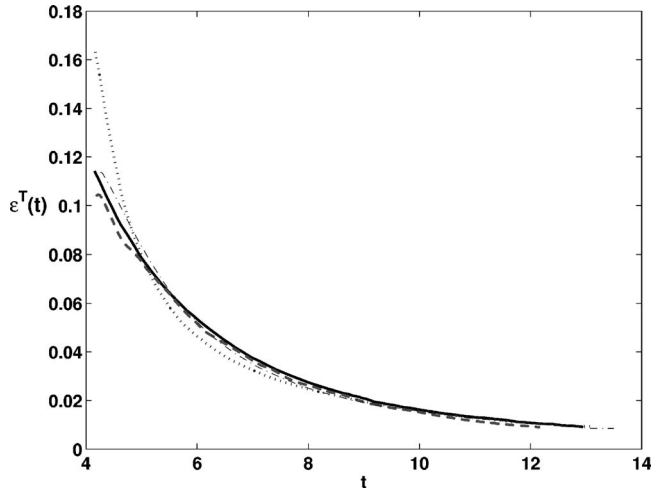

FIG. 17. Total resolved-scale energy dissipation, including total subgrid energy production and resolved-scale viscous dissipation, from decaying test case in Sec. VI, comparing filtered DNS result (solid) with LES results using multifractal subgrid-scale model (dashed), dynamic Smagorinsky model (dashed-dotted) and conventional Smagorinsky model (dotted).

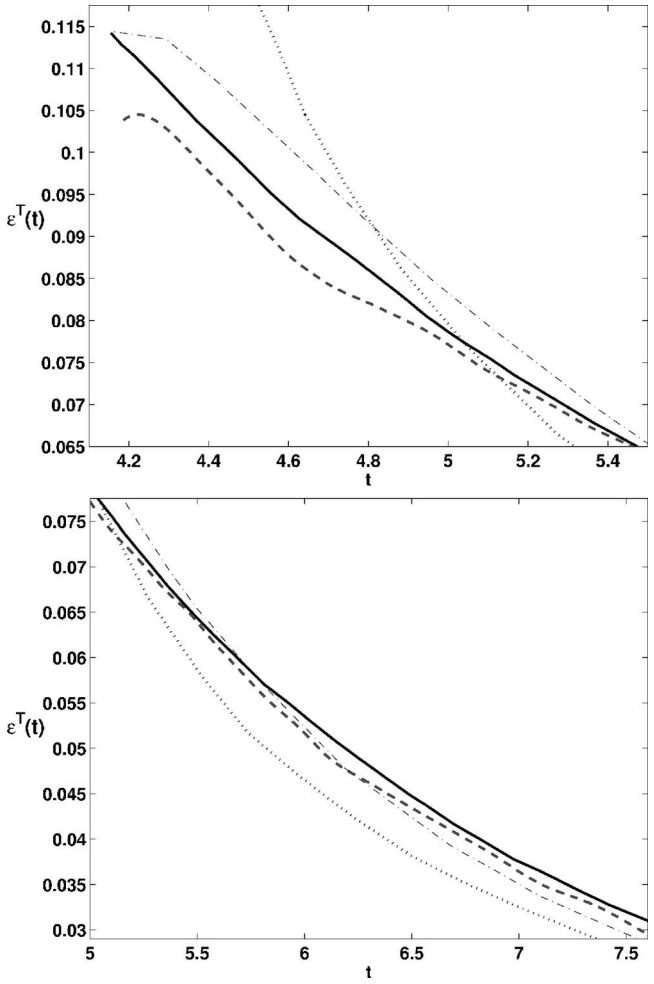

FIG. 18. Details of energy dissipation profile in Fig. 17 at start of decay (top) and at intermediate stage (bottom), showing comparisons of filtered DNS result (solid) with LES results using multifractal subgrid-scale model (dashed), dynamic Smagorinsky model (dashed-dotted) and conventional Smagorinsky model (dotted). Note multifractal model adjusts rapidly from initial condition and subsequently follows DNS result closely.

obtained from the dynamic Smagorinsky model, with the same two-dimensional intersection shown in Figs. 2 and 7. Figures 2, 7, and 20 thus allow direct comparisons of the filtered DNS result for $\mathcal{P}(\mathbf{x},t)$, the corresponding $\mathcal{P}(\mathbf{x},t)$ from the present multifractal model, and the $\mathcal{P}(\mathbf{x},t)$ from the dynamic Smagorinsky model. While the dynamic Smagorinsky model provides sufficient total dissipation to allow the overall energy in the flow in Fig. 14 to be simulated, it provides a very poor representation of the spatial structure in the energy exchange between the resolved and subgrid scales. The same is true in the bottom panel in Fig. 20 for the corresponding $\mathcal{P}(\mathbf{x},t)$ from the scale-similarity model of Bardina *et al.*[18] While that model allows for backscatter that gives phase correlations of roughly 0.65 with corresponding DNS fields, the resulting average subgrid energy transfer $\langle\mathcal{P}(\mathbf{x},t)\rangle$ is far too low. When used in a "mixed" model with an eddy-viscosity part like the Smagorinsky model to give the correct $\langle\mathcal{P}\rangle$, it provides essentially no fidelity in representing the spatial structure in the energy exchange between the resolved and subgrid scales. By comparison, $\mathcal{P}(\mathbf{x},t)$ from the multifractal model in Fig. 2, even with the backscatter limiting shown in Fig. 7, provides excellent agreement with the filtered DNS result for $\mathcal{P}(\mathbf{x},t)$ in Fig. 2.

These simulations of decaying turbulence show that the multifractal subgrid-scale model and the backscatter limiter are capable of providing accurate large-eddy simulations of flows in which the subgrid properties undergo significant change. In such cases, the subgrid model that provides for exchange of momentum and energy between the resolved and subgrid scales, as well as the method used to remove any unphysical energy to maintain stability of the solver, must correctly adjust to these changes in the subgrid turbulence properties. In most approaches for subgrid-scale modeling, these two aspects of LES have been lumped together, with the consequence that fidelity in $\mathcal{P}(\mathbf{x},t)$ is largely abandoned in order to obtain stability in the solver. Consequently, most attention to date has focused on global properties of the energetics associated with various SGS models. The present results show that, even in a decaying flow with large changes in the subgrid properties, it is possible for physically-based approaches like the multifractal model with the backscatter limiter to provide stability via removal of the unphysical energy, while at the same time providing high fidelity in representing the detailed spatial structure of the momentum and energy exchange between the resolved and subgrid scales.

VII. CONCLUDING REMARKS

This study has conducted *a posteriori* evaluations of the multifractal subgrid-scale model developed in Part I which show that stable and accurate large-eddy simulations can be obtained when this model is used to represent the subgrid-scale turbulence physics, and when the present backscatter limiter is used to remove the spurious energy introduced in the resolved scales by the numerics of the flow solver. This contrasts with previous approaches in which the subgrid turbulence model has been used principally to stabilize the

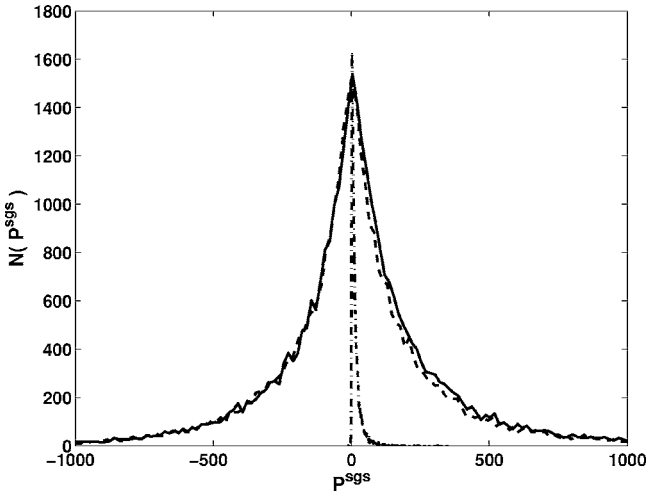

FIG. 19. Distribution of subgrid energy production $\mathcal{P}(\mathbf{x},t)$ from filtered DNS data (solid) compared with multifractal model (dashed) and dynamic Smagorinsky model (dashed-dotted). Note dynamic Smagorinsky model only approximates net transfer of energy to the subgrid scales; multifractal model additionally provides local forward and backward energy transfer between resolved and subgrid scales.

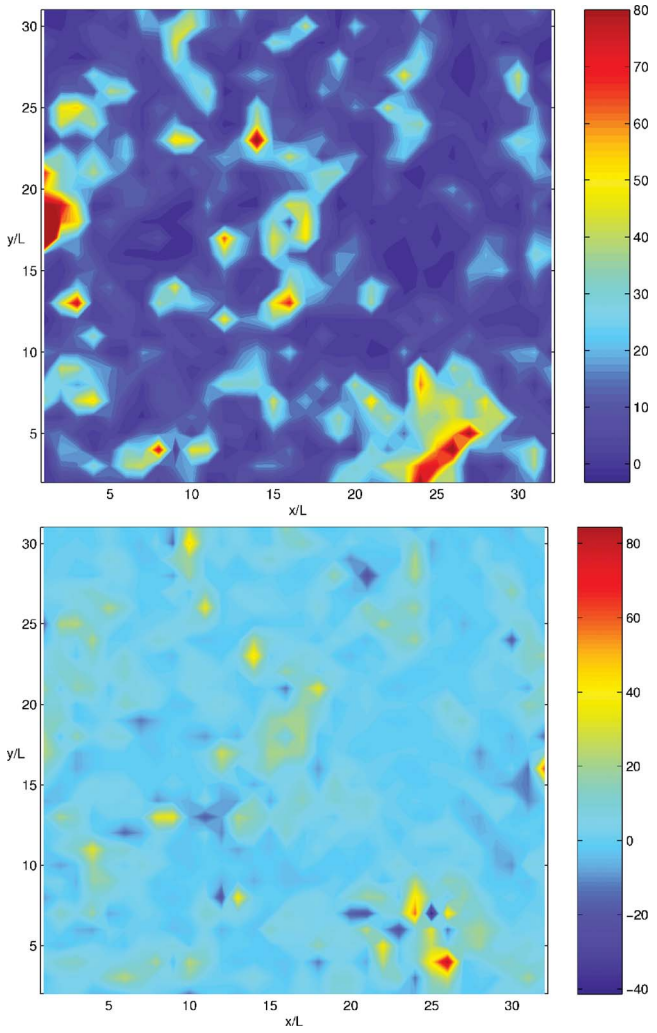

FIG. 20. (Color). Subgrid energy production fields $\mathcal{P}(\mathbf{x},t)$ from dynamic Smagorinsky model (top) and Bardina scale-similarity model (bottom), showing same intersection as in Fig. 2 (top and bottom) to allow direct comparison with corresponding result from multifractal model and with actual $\mathcal{P}(\mathbf{x},t)$ from filtered DNS. Note only multifractal subgrid-scale model provides any significant fidelity in representing detailed spatial structure of momentum and energy exchange between resolved and subgrid scales.

computations by dissipating this spurious energy or merely to represent the average net flux of energy to the subgrid scales, rather than as a means for representing the subgrid production field $\mathcal{P}(\mathbf{x},t)$ with any significant degree of fidelity. Here the physical subgrid-scale model provides a high-fidelity representation of the detailed spatial and temporal structure in the momentum and energy transfer between the subgrid and resolved scales, while the backscatter limiter controls the numerical errors separately in a manner that does not sacrifice the fidelity in the $\tau_{ij}(\mathbf{x},t)$ and $\mathcal{P}(\mathbf{x},t)$ fields. The multifractal subgrid-scale model and the backscatter limiter allow these two aspects of any accurate large-eddy simulation to be accomplished without incurring a substantially greater computational burden than do widely used dynamic eddy-viscosity approaches, in which these two functions are tightly coupled and which therefore provide much lower fidelity in representing $\tau_{ij}(\mathbf{x},t)$ and $\mathcal{P}(\mathbf{x},t)$.

Large-eddy simulations with the multifractal subgrid-scale model are based on the momentum equation in (7), which involves both the subgrid stress τ_{ij}^{*} in (8) and the resolved stress $\overline{\overline{u}_i\overline{u}_j}$. The subgrid stress $\tau_{ij}^{*}(\mathbf{x},t)$ is evaluated from (14)–(22), obtained as described in Part I from a multifractal representation of the subgrid vorticity field. This was shown by *a priori* tests in Part I to provide remarkably accurate representations for the filtered subgrid velocities $u_i^{sgs}(\mathbf{x},t)$, the associated subgrid stress components $\tau_{ij}^{*}(\mathbf{x},t)$, and the subgrid part $\mathcal{P}^{*}(\mathbf{x},t)$ of the subgrid energy production field. The resolved stress $\overline{\overline{u}_i\overline{u}_j}(\mathbf{x},t)$ is evaluated from (19) with the same explicit filter used in the evaluation of τ_{ij}^{*}. This was here shown to provide highly accurate representations for the resolved part $\mathcal{P}^{R}(\mathbf{x},t)$ of the subgrid energy production field $\mathcal{P}(\mathbf{x},t)$, with resulting correlations between model values and filtered DNS values in Table I exceeding 99%.

The backscatter limiter developed here, which removes the spurious energy introduced by numerical errors, makes only small reductions to the backscatter components $\mathcal{P}_{(ij)}(\mathbf{x},t)$ in (25) where gradients in the resolved field are large, and thus where the spurious energy is presumably also largest. This is readily implemented in (7) by reducing the corresponding components $\tau_{(ij)}^{*}$ and $\overline{u}_{(i)}\overline{u}_{(j)}$ by the factor $C_{\mathcal{B}}$ as in (30) and (31). While the backscatter coefficient $C_{\mathcal{B}}$ has here been taken as spatially uniform, the amount of reduction of the backscatter components in (28) depends on the magnitude of each component, and thus varies throughout the flow.

When this backscatter limiter was combined with the multifractal subgrid-scale model in a flow solver and used for *a posteriori* evaluations, the resulting large-eddy simulations were found to provide stable and accurate results in long time-integrations of forced homogeneous isotropic turbulence simulations on a 32^3 grid with cell Reynolds numbers ranging from $160 \leqslant Re_{\Delta} \leqslant 10^6$. For the $Re_{\Delta} \approx 160$ case, the availability of filtered DNS results on the same 32^3 grid allowed for detailed comparisons to assess the accuracy of

these LES calculations with the multifractal subgrid-scale model. Comparisons of probability densities for the velocity gradient components $\partial\overline{u}_i/\partial x_j$ showed good agreement of the LES results with corresponding filtered DNS results. Even the intermittent large-gradient features in the resolved fields, produced by the nonlinear steepening of resolved-scale gradient quantities into concentrated structures by locally high strain rates in both the resolved and subgrid fields, were accurately reproduced in these LES results with the multifractal subgrid-scale model. Various statistical moments of these probability densities were found to agree to within a few percent with the corresponding filtered DNS values and with theoretical values for homogeneous isotropic turbulence, approaching the limits of statistical uncertainty in such comparisons. Similar comparisons of resolved-scale stress components $\overline{u}_i\overline{u}_j$, resolved-scale enstrophy values, and viscous dissipation rates in the resolved scales showed good agreement with corresponding filtered DNS results. Additionally, the present LES results for the decaying homogeneous isotropic turbulence case show that, even under conditions for which the subgrid properties undergo significant changes over the course of the simulation, the multifractal subgrid model and the backscatter limiter provide accurate results. Collectively the results from these *a posteriori* assessments support the conclusion that the multifractal subgrid-scale model developed in Part I and the backscatter limiter developed here allow for stable and accurate large-eddy simulations of turbulent flows.

Obvious extensions of this multifractal subgrid-scale model include the development of corresponding subgrid models for conserved scalar transport, using an analogous procedure based on the multifractal structure in scalar gradient-magnitude fields[29,30] at inertial-range scales of high Reynolds number turbulent flows. In this case, an analogous multiplicative cascade would provide the multifractal representation for the subgrid scalar-gradient magnitude, and an analogous additive cascade would provide a corresponding representation for the progressively isotropic decorrelation of the scalar-gradient orientation as the cascade proceeds from the grid-scale Δ to the corresponding inner (diffusion) scale λ_D in the subgrid scalar field. The resulting subgrid scalar-gradient field would then be related to the subgrid scalar field via a Green's function integral that allows for an evaluation similar to that used in Part I for the Biot–Savart integral that relates the subgrid velocity to the subgrid vorticity. The similarity between the multifractal model for the subgrid vorticity field developed in Part I and a corresponding multifractal model for the subgrid scalar-gradient field to give the subgrid scalar field and the associated subgrid scalar flux components needed for LES of scalar mixing problems suggests that this extension should be largely straightforward.

A further obvious extension of the present multifractal subgrid-scale model is to wall-bounded turbulent flows, for which the cell Reynolds number Re_Δ decreases as the wall is approached and the underlying vorticity field becomes highly anisotropic in the near-wall region. Both of these factors will affect the evaluation of the Biot–Savart integral. The former decreases the number $N=(\Delta/\lambda_\nu)^3$ of inner-scale cells of size λ_ν within each resolved-scale grid cell of size Δ, and the latter will introduce strong correlations in the orientation of the subgrid vorticity within the grid cells. However, precisely these considerations naturally suggest specific ways in which the derivation in Part I may be modified to provide a rational approach to developing such a near-wall limit of the present modeling approach, in place of the various *ad hoc* wall functions that are customarily introduced to modify traditional eddy-viscosity models for use in the near-wall region. Extensions of the present multifractal subgrid-scale model to permit such use in near-wall turbulence may thus also be relatively straightforward.

ACKNOWLEDGMENTS

Discussions with K. Powell and D. Dowling at Michigan are gratefully acknowledged. The authors express their gratitude to Dr. Thomas Lund for providing the original LES code used in this work, and to Professor Thomas Hughes and Dr. Alan Wray for providing data from their simulations of decaying turbulence. This work was jointly supported, in part, by the National Aeronautics and Space Administration (NASA) Marshall and Glenn Research Centers and the Department of Defense (DoD) within the NASA Constellation University Institutes Project (CUIP) Space Vehicle Technology Institute (SVTI) under Grant No. NCC3-989, with Claudia Meyer as the project manager. G.C.B. gratefully acknowledges the generous financial support of the François-Xavier Bagnoud Fellowship provided by the Association François-Xavier Bagnoud of Sion, Switzerland.

[1] G. C. Burton and W. J. A. Dahm, "Multifractal subgrid-scale modeling for large-eddy simulation. I. Model development and *a priori* testing," Phys. Fluids **17**, 075111 (2005).
[2] T. S. Lund, "The use of explicit filters in large eddy simulation," Comput. Math. Appl. **46**, 603 (2003).
[3] A. Leonard, "Energy cascade in large-eddy simulations of turbulent fluid flows," Adv. Geophys. **18A**, 237 (1974).
[4] D. K. Lilly, "The representation of small-scale turbulence in numerical simulation experiments," in *Proceedings of the IBM Scientific Computing Symposium on Environmental Sciences*, Yorktown Heights, New York (1967).
[5] J. W. Deardorff, "A numerical study of three-dimensional turbulent channel flow at large Reynolds numbers," J. Fluid Mech. **41**, 453 (1970).
[6] R. A. Clark, J. H. Ferziger, and W. C. Reynolds, "Evaluation of subgrid-scale models using an accurately simulated turbulent flow," J. Fluid Mech. **91**, 1 (1979).
[7] N. N. Mansour, P. Moin, W. C. Reynolds, and J. H. Ferziger, "Improved methods for large eddy simulations of turbulence," in *Turbulent Shear Flows I*, edited by F. Durst *et al.* (Springer-Verlag, Berlin, 1979).
[8] M. Antonopoulos-Domis, "Large-eddy simulation of a passive scalar in isotropic turbulence," J. Fluid Mech. **104**, 55 (1981).
[9] R. S. Rogallo and P. Moin, "Numerical simulation of turbulent flows," Annu. Rev. Fluid Mech. **16**, 99 (1984).
[10] G. S. Winckelmans, T. S. Lund, D. Carati, and A. A. Wray, "*A priori* testing of subgrid-scale models for the velocity-pressure vorticity-velocity formulations," in *Proceedings of the Summer Program, Center for Turbulence Research*, Stanford University (1996).
[11] G. S. Winckelmans, H. Jeanmart, and D. Carati, "On the comparison of turbulence intensities from large-eddy simulation with those from experiment or direct numerical simulation," Phys. Fluids **14**, 1809 (2002).
[12] B. Knaepen, O. Debliquy, and D. Carati, "Subgrid-scale energy pseudo pressure in large-eddy simulation," Phys. Fluids **14**, 4235 (2002).
[13] U. Piomelli, W. H. Cabot, P. Moin, and S. Lee, "Subgrid-scale backscatter in turbulent and transitional flows," Phys. Fluids A **3**, 1766 (1991).
[14] S. K. Lele, "Compact finite difference schemes with spectral-like resolution," J. Comput. Phys. **103**, 16 (1992).
[15] S. Ghosal, "An analysis of numerical errors in large-eddy simulations of

turbulence," J. Comput. Phys. **125**, 187 (1996).
[16] A. G. Kravchenko and P. Moin, "On the effect of numerical errors in large eddy simulations of turbulent flows," J. Comput. Phys. **131**, 310 (1997).
[17] F. K. Chow and P. Moin, "A further study of numerical error in large-eddy simulations," J. Comput. Phys. **184**, 366 (2003).
[18] J. Bardina, J. H. Ferziger, and W. C. Reynolds, "Improved turbulence models based on large eddy simulation of homogeneous, incompressible, turbulent flows," Technical Report TF-19, Thermosciences Division, Stanford University, Stanford, CA (1983).
[19] C. E. Leith, "Stochastic in a subgrid-scale model—plane shear mixing layer," Phys. Fluids A **2**, 297 (1990).
[20] M. Germano, U. Piomelli, P. Moin, and W. H. Cabot, "A dynamic subgrid-scale eddy viscosity model," Phys. Fluids A **3**, 1760 (1991).
[21] J. R. Chasnov, "Simulation of the Kolmogorov inertial subrange using an improved subgrid model," Phys. Fluids A **3**, 188 (1991).
[22] S. Ghosal, T. S. Lund, P. Moin, and K. Akselvoll, "A dynamic localization model for large-eddy simulation of turbulent flows," J. Fluid Mech. **286**, 229 (1995).
[23] D. Carati, S. Ghosal, and P. Moin, "On the representation of backscatter in dynamic localization models," Phys. Fluids **7**, 606 (1995).
[24] F. H. Harlow and J. E. Welch, "Numerical calculation of time-dependent viscous incompressible flow of fluids with free surface," Phys. Fluids **8**, 2182 (1965).
[25] P. R. Spalart, R. D. Moser, and M. M. Rogers, "Spectral methods for the Navier–Stokes equations with one infinite and two periodic directions," J. Comput. Phys. **96**, 297 (1991).
[26] S. Liu, C. Meneveau, and J. Katz, "On the properties of similarity subgrid-scale models as deduced from measurements in a turbulent jet," J. Fluid Mech. **275**, 83 (1994).
[27] T. J. R. Hughes, L. Mazzei, A. A. Oberai, and A. A. Wray, "The multiscale formulation of large eddy simulation: Decay of homogeneous isotropic turbulence," Phys. Fluids **13**, 505 (2001).
[28] H. S. Kang, S. Chester, and C. Meneveau, "Decaying turbulence in an active-grid-generated flow comparisons with large-eddy simulation," J. Fluid Mech. **480**, 129 (2003).
[29] R. D. Frederiksen, W. J. A. Dahm, and D. R. Dowling, "Experimental assessment of fractal scale similarity in turbulent flows. Part 3. Multifractal scaling," J. Fluid Mech. **338**, 127 (1997).
[30] R. D. Frederiksen, W. J. A. Dahm, and D. R. Dowling, "Experimental assessment of fractal scale similarity in turbulent flows. Part 4. Effects of Reynolds Schmidt numbers," J. Fluid Mech. **377**, 169 (1998).